On Horizontal Axis Wind Turbines Design, Optimization and CFD Analysis

Clemente J. Juan Oliver

Supervised by:
Pedro Manuel Quintero Igeño

A project presented for the degree of
Aerospace Engineer

Escuela Técnica Superior de Ingeniería del Diseño

Universitat Politècnica de València
Valencia, Spain
November 2020

Resumen

El uso de la energía eólica para la generación de energía es cada vez más atractivo y está ganando una gran participación en el mercado de producción de electricidad en todo el mundo.

En este estudio se podrán ver los diferentes pasos que hay que dar para diseñar y analizar un aerogenerador, pudiendo ver qué cosas merecen la pena tener en cuenta, qué problemas pueden surgir y cómo solucionarlos. Además, se identificarán los puntos óptimos de operación, pudiendo ofrecer un rango de trabajo en el que la turbina obtendrá la máxima potencia manteniendo una producción segura y mínimos gastos de mantenimiento.

Se observarán los efectos de varios parámetros básicos de diseño teóricamente, así como las ventajas y desventajas de las suposiciones realizadas. Al final, una vez sentadas las bases teóricas, se realizará un modelado fluidodinámico para que el análisis de Dinámica de Fluidos Computacional (CFD por sus siglas en inglés) estudie más en profundidad los fenómenos que rodean estos casos, averiguando cuáles son los aspectos más importantes, y hasta qué punto la teoría o el CFD es capaz de predecir algunos de estos efectos.

Además, este documento tiene la intención de proporcionar un punto de vista ilustrativo sobre el análisis CFD de una forma aerodinámica, que podría resultar útil para otros estudiantes, investigadores o incluso personas aficionadas al tema.

Abstract

The use of wind energy for power generation purposes is becoming increasingly attractive and gaining a great share in the electrical power production market worldwide.

In this study, one will get to see the different steps that have to be made in order to design and analyse a wind turbine, being able to see which things are worth taking into account, and which problems may arise and how to solve them. In addition, the optimum operation points will be identified, being able to offer a range of operation in which the wind turbine will obtain the maximum power while keeping a safe operation and minimum maintenance costs.

The effects of several core design parameters will be observed theoretically, as well as the pros and drawbacks of the assumptions made. In the end, once the theoretical background has been determined, a fluid dynamic modelling will be carried out and the Computational Fluid Dynamics (CFD) analysis will study more in deep the phenomena surrounding these cases, finding out which are the most important aspects, and up to which point theory or CFD is able to predict some effects.

Moreover, this document intends to provide an illustrative point of view on CFD analysis of an aerodynamic shape, which might prove useful to any other students, researchers or even intriguing people.

Contents

i

List of Figures

List of Tables

1 Introduction

In Spain 16% of electricity demand is met by wind, and at times provides over half the electricity needed. The European Commission believes wind energy will supply 25% of the EU's electricity by 2025 and between 32% and 49% by 2050[1]. The key will be a Europe-wide power grid which will transport wind energy from where it is produced to where it is consumed, needing a well-optimized field of wind turbine.

Since the energy model changing cycles are quite long and involve a high initial investment, it is necessary to consider the long term. The objective would be to have a globalized, decentralized and non-polluting electrical network, without sacrificing quality, safety and a continuous access to it (not depending on conflicts between countries, meteorological events, etc). This means reaching important international agreements, as well as maintaining a balance that guarantees investment without falling into a lack of regulation that could lead to monopolies. There are two levels of scope of any project of this type: a local one more focused on generation and more immediate transportation, and another that ensures the connection of different more distant points, which needs, as already mentioned, an important cooperation.

According to `windeurope.org`[1], Spain installed 2.3 GW of onshore wind, 15% of all new wind capacity in Europe last year. This is its highest volume since 2009. Most of the installed capacity was presented in the 2016 and 2017 auctions, when more than 4 GW of wind energy projects were approved. The remaining capacity from those auctions should be build in 2020. Moreover Figure 1.1 illustrates how 55% of new wind power in Europe was installed just in four countries: the UK, Spain, Germany and Sweden.

MW		UK	Spain	Germany	Sweden	France	Norway	Greece	Turkey	Ukraine	Belgium	Ireland	Italy	Denmark	Finland	Others
	Offshore	1,764	-	1,111	-	-	-	-	-	-	370	-	-	374	-	8
	Onshore	629	2,319	1,078	1,588	1,336	780	727	686	637	207	463	456	28	243	563
	Total	2,393	2,319	2,189	1,588	1,336	780	727	686	637	577	463	456	402	243	571
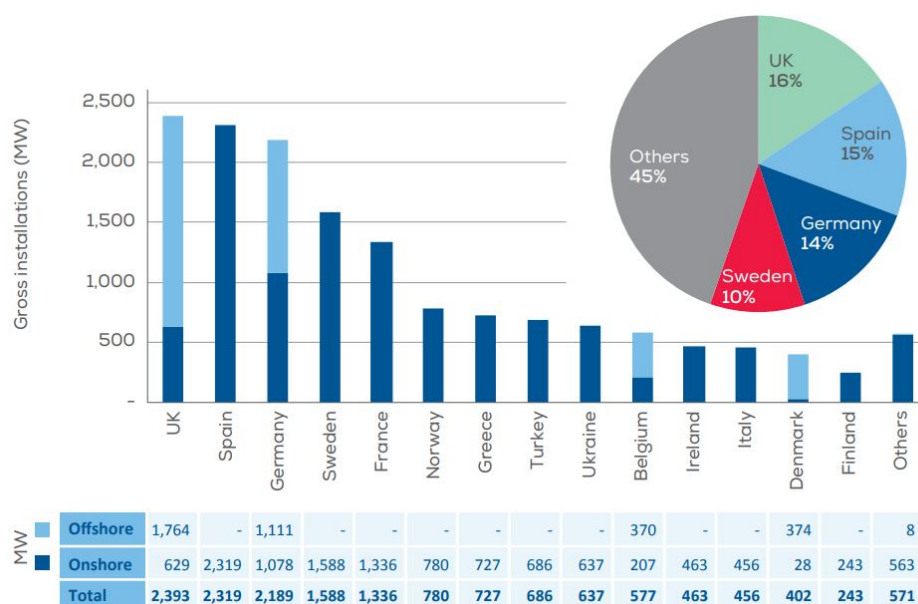
Figure 1.1: 2019 new onshore and offshore wind installations in Europe
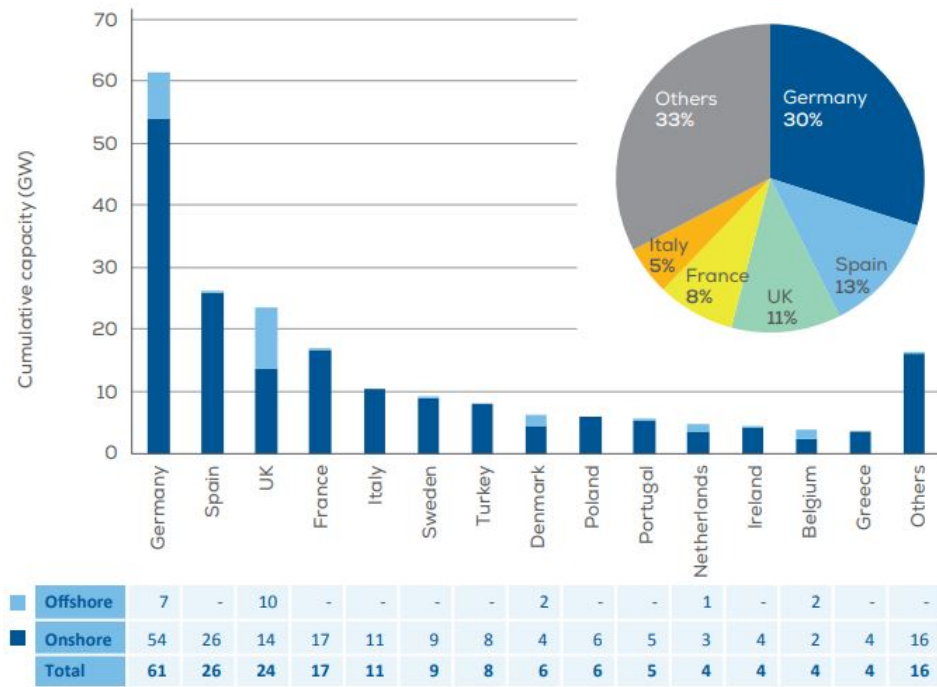
Figure 1.2: Total installed wind power capacity by country

In total 205 GW of wind power capacity are now installed in Europe (Figure 1.2)[1], from which 89% of this is onshore and 11% of it is offshore. Germany remains the country with the largest installed capacity in Europe, followed by Spain, the UK, France and Italy.

By reading this, one realizes wind turbines industry is growing each year, being onshore wind the cheapest form of new power generation in Europe nowadays, which makes it essential to develop research tools and validations for new designs, however, experiments cannot always be carried, so the widely used alternative is CFD.

For this project the Star-CCM+ program was used, offering a versatile range of options and tools for the study of fluid interaction and behaviour with the blades, which in addition to the benefits from the economic point of view (testing a 20 m wind turbine is not always physically feasible), makes it an essential tool not only for designing these type of rotors, but for many other engineering problems and fields. The workflow of the CFD analysis that will be followed in this project is illustrated in Figure 1.3.

In addition, Matlab was used as well, a very popular program which allows matrix manipulations, plotting of functions and data, implementation of algorithms, creation of user interfaces, and interfacing with programs written in other languages, so in this case it was used in order to manage and plot data extracted from Star-CCM+ so that it could be easier to work with as well as providing a better-looking result. Of course, regarding data management, Microsoft Excel was used as well to carry out some calculations and graphs.

2
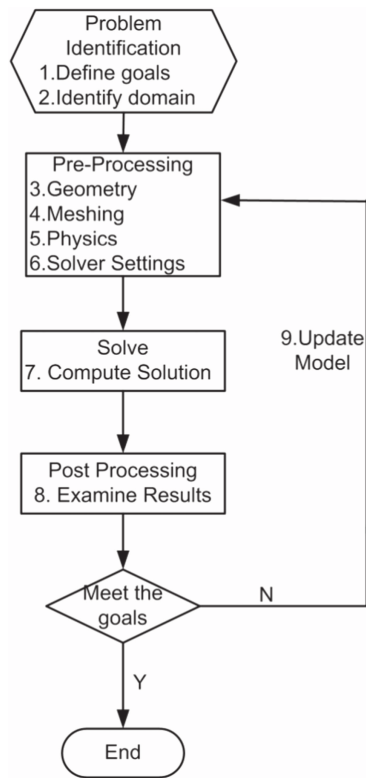
Figure 1.3: Workflow of the CFD simulation

2 Fundamentals of Aerodynamics, Mechanics and Dynamics of Wind Turbines

2.a General Overview

Horizontal axis wind turbines transform wind into useful energy making use of a well designed blade. This section will provide with a theoretical background in order to better understand the energy transformation that takes place and how power generation can be optimized thanks to the airfoil and blade design analysis.

For the current objective, only the aerodynamic forces generated by an steady blow of wind will be considered, not taking into account the small variations with time. However, a brief introduction to unsteady rotor performance will be given at the beginning of Section 3.f.

Since the analysis carried out by Betz [2] and Glauert [4] in the 1920s and 1930s, theory on the analysis of wind turbines is being developed and expanded widely, but this section will try to explain all these concepts in the most accessible way to readers without any engineering background following the concepts and equations stated by Manwell et al.[5].

2.b One-dimensional Approach

In 1919, Albert Betz, a German phycisist, stated that the maximum power that can be extracted from the wind has a theoretical limit[3]. In order to prove it, he made use of a simple one-dimensional model based on linear momentum theory, which can be also used to make a first approximation of the power a horizontal axis wind turbine can produce.

This model assumes a control volume in which a wind entrance and exit are bounded by the surface of a stream tube, being the wind turbine an 'actuator disk' that represents an infinite number of blades and consequently a pressure drop in the air flow (see Figure 2.1).
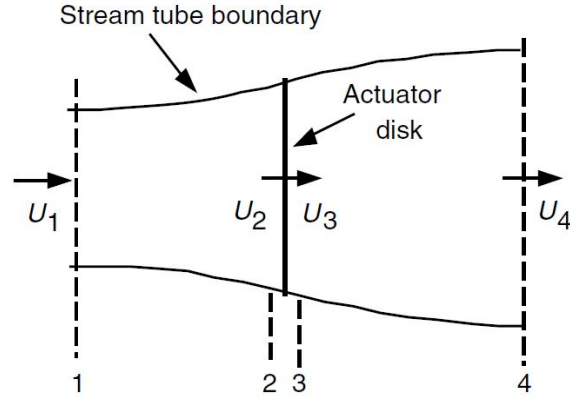
Figure 2.1: Actuator disk model of a wind turbine; U, mean air velocity; 1, 2, 3, and 4 indicate locations

The analysis takes the following considerations: homogeneous, incompressible, steady state fluid flow with no drag nor viscous effects, an infinite number of blades, non-rotating wake, uniform thrust around the disk and the static pressure far upstream and downstream (locations 1 and 4) is the ambient one.

Applying the conservation of linear momentum equation in the control volume the net force of the wind turbine is equal and opposite to the thrust the blades generate:

$$T = U_1(\rho A U)_1 - U_4(\rho A U)_4 \tag{2.1}$$

where ρ is the air density, A is the cross-sectional area, U the air velocity and the numbers indicate the locations in the model of Figure 2.1. Moreover, since the mass flow ($\dot{m} = \rho A U$) can be considered constant along the tube (the same amount of air that enters the control volume exits it), Equation 2.1 can be rewritten as:

$$T = \dot{m}(U_1 - U_4) \tag{2.2}$$

In Equation 2.2 the thrust can be considered positive, so the free stream velocity (U_1) will be reduced when passing through the actuator disk and therefore U_4 will be less than U_1.

If the velocity around the turbine rotor is taken as constant ($U_2 = U_3$) and no work is done on either side of the actuator disk, the Bernoulli equation can be written for both sides of the actuator disk like:

5

$$p_1 + \frac{1}{2}\rho U_1^2 = p_2 + \frac{1}{2}\rho U_2^2 \tag{2.3}$$

$$p_3 + \frac{1}{2}\rho U_3^2 = p_4 + \frac{1}{2}\rho U_4^2 \tag{2.4}$$

and expressing the thrust as the net sum of forces on each side (Equation 2.5):

$$T = A_2(p_2 - p3) \tag{2.5}$$

One can solve $p_2 - p_3$ from Equations 2.3 and 2.4 and substitute it on Equation 2.5, obtaining:

$$T = \frac{1}{2}\rho A_2(U_1^2 - U4^2) \tag{2.6}$$

Here making use of Equation 2.2 the following relation appears (Equation 2.7):

$$U_2 = U_3 = \frac{U_1 + U_4}{2} \tag{2.7}$$

Then, introducing the axial induction factor, a , as a decelerating coefficient between U (free stream velocity) and U_2 (around the rotor):

$$U_2 = U_1(1 - a) \tag{2.8}$$

and

$$U_4 = U_1(1 - 2a) \tag{2.9}$$

So a must be under 0.5 in order for the wind to keep some velocity at U_4

On the other hand, the power generated, P, can be expressed as the thrust times the velocity at the turbine rotor, U_2:

$$P = \frac{1}{2}\rho A_2(U_1^2 - U_4^2)U_2 \tag{2.10}$$

where A_2 (control volume area at the disk) can be substituted by A (the rotor area), and the free stream velocity (U_1) by U. Then one can rearrange Equation 2.10 with the help of Equations 2.8 and 2.9:

$$P = \frac{1}{2}\rho AU^3 4a(1-a)^2 \tag{2.11}$$

For the aim of improving the performance of a wind turbine, the non-dimensional power coefficient (C_P) plays a major role, since the generated power can also be expressed as $P \propto C_P U^3$, and the turbine performance is usually characterized by this coefficient. It also has an important effect in controllability at extreme wind speeds, and represents the coefficient of the rotor power against the power in the wind:

$$C_P = \frac{P}{\frac{1}{2}\rho AU^3} \tag{2.12}$$

$$C_P = 4a(1-a)^2 \tag{2.13}$$

Taking the derivative with respect to a and equalizing it to zero, which yields $a = 1/3$, will maximize C_P, obtaining the value:

$$C_P = \frac{16}{27} = 0.5926 \tag{2.14}$$

This value is known as Betz's limit, and states that if an ideal turbine rotor was designed and operated such that the wind speed at the rotor (U_2) was 2/3 of the free stream wind speed (U), then it would be operating at the point of maximum power production, since no turbine can capture more than 59.26% of the kinetic energy in wind.

Working similarly to Equation 2.11, the thrust on the rotor is:

$$T = \frac{1}{2}\rho A U^2 4a(1-a) \tag{2.15}$$

And the non-dimensional normal force can be expressed as the coefficient between the thrust force and the dynamic force:

$$C_T = \frac{T}{\frac{1}{2}\rho A U^2} \tag{2.16}$$

Operating with Equations 2.15 and 2.16 and maximizing like in Equation 2.13 , the maximum achievable thrust coefficient is equal to 1, for $a = 1/2$. Note that for the maximum achievable $C_P = 16/27$, $a = 1/3$ and C_T is equal to 8/9. One must bear in mind that any axial induced factor over 1/2 yields invalid results due to wrong or complicated results of air velocity behind the rotor (U_4), which cannot be studied using this simplified model. This is represented graphically in Figure 2.2, where the maximum values are easily located. Above $a = 1/2$, in the turbulent wake state, measured data indicate that thrust coefficients increase up to about 2.0 at an axial induction factor of 1.0. This state is characterized by a large expansion of the slipstream, turbulence and recirculation behind the rotor. While momentum theory no longer describes the turbine behavior, empirical relationships between C_T and the axial induction factor are often used to predict wind turbine behavior[5].
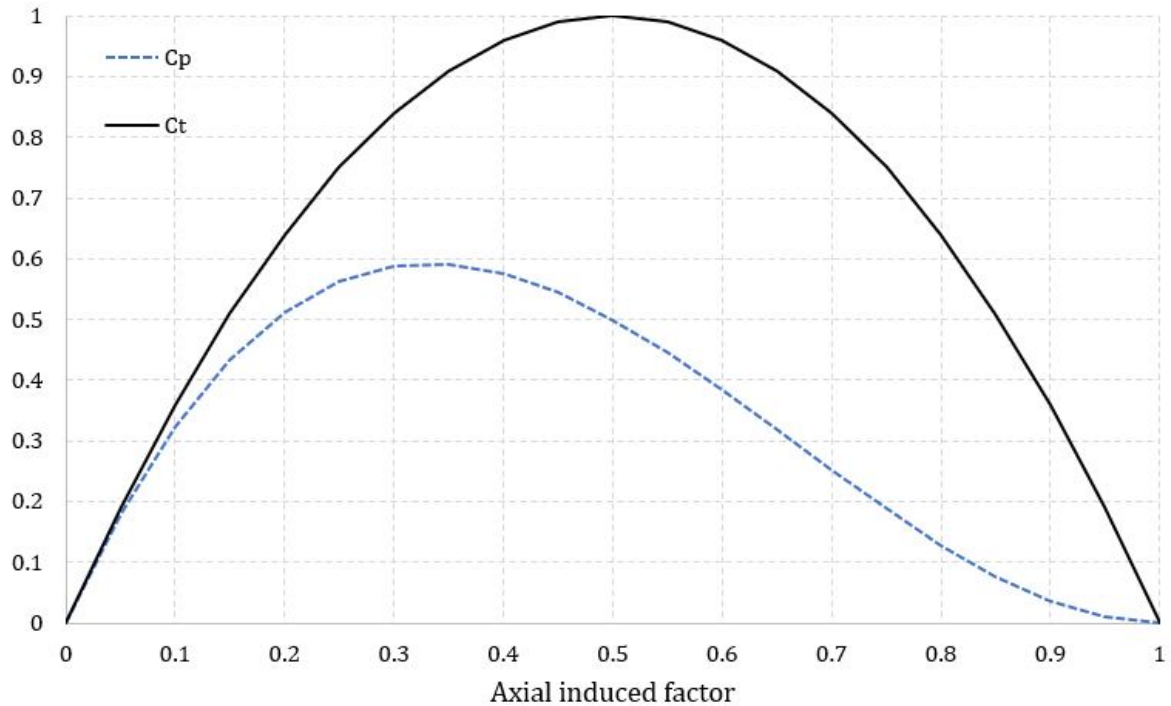
Figure 2.2: Operating parameters C_P and C_T for a Betz turbine

In practice, some real effects that were simplified in this model greatly decrease the performance of the turbine, so in order to measure the effect on the power coefficient of these phenomena some in depth study must be made on three main effects (apart from mechanical losses): rotation of the wake behind the rotor, finite number of blades (and associated tip losses) and aerodynamic drag.

2.c   Horizontal Axis Wind Turbine with Wake Rotation

In this subsection the wake rotation is included in the simplified model of the previous part. This flow rotation is in the opposite direction of the turbine rotation, as a reaction to the torque applied from the wind to the blades (see Figure 2.3).

9
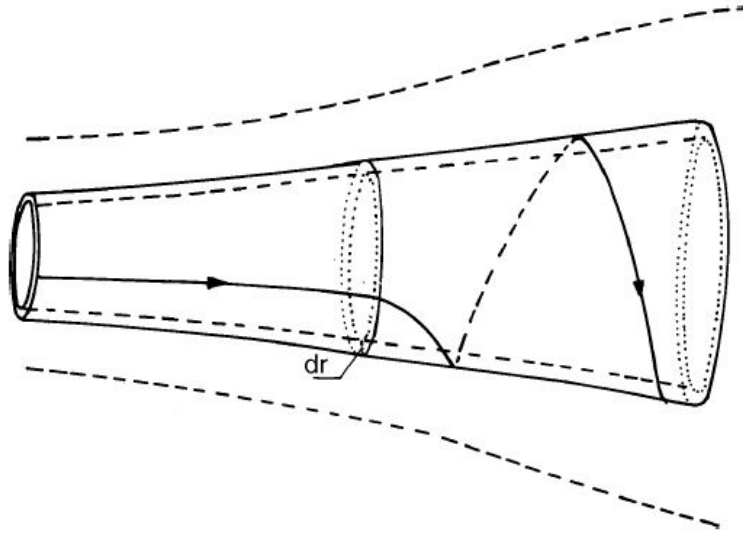
Figure 2.3: Picture of stream tube with wake rotation

Due to this wake, there will be less energy to extract from the wind than in the previous case, and as will be shown in this Section, wind turbines with low rotational speed and high torque have more wake losses than high-speed wind ones with low torque.

Taking the pressure, wake rotation and induction factors as a function of the radius, and assuming ω (angular velocity of the flow) is much smaller than Ω (angular velocity of the rotor) as well as that the pressure in the far wake equal to the free stream pressure, one can use a control volume with a cross-sectional area equal to $2\pi r dr$ (circumference of width dr) that yields the following relation of pressures (see Glauert, 1935 [4])):

$$p_2 - p_3 = \rho(\Omega + \frac{1}{2}\omega)\omega r^2 \qquad (2.17)$$

Notice that the increment of the angular velocity of the flow relative to the blade in the actuator disk increases from Ω to $\Omega + \omega$, while the axial component remains constant. Then using the definition of the thrust applied to an annular element:

$$dT = (p_2 - p_3)dA = \left[\rho(\Omega + \frac{1}{2}\omega)\omega r^2\right] 2\pi r dr \qquad (2.18)$$

Here the angular induced factor can be expressed as:

10

$$a' = \omega/2\Omega \tag{2.19}$$

And when including the wake rotation, a rotor plane component appears, $r\Omega a'$. So Equation 2.18 can be rewritten as:

$$dT = 4a'(1 + a')\frac{1}{2}\rho\Omega^2 r^2 2\pi r dr \tag{2.20}$$

Analogously, thrust can also be expressed using the axial induced factor a, being U the free stream velocity U_1:

$$dT = 4a(1 - a)\frac{1}{2}\rho U^2 2\pi r dr = 4a(1 - a)\rho U^2 \pi r dr \tag{2.21}$$

Making these two thrusts (Equations 2.20 and 2.21) equal gives the local tip speed ratio (λ_r) definition:

$$\frac{a(1 - a)}{a'(1 + a')} = \frac{\Omega^2 r^2}{U^2} = \lambda_r^2 \tag{2.22}$$

Using the expression of λ_r for the whole blade, the non-dimensional tip speed ratio (λ) is introduced:

$$\lambda = \frac{\Omega R}{U} \tag{2.23}$$

And Equations 2.22 and 2.24 can be related in the following way:

$$\lambda_r = \frac{\Omega r}{U} = \lambda\frac{r}{R} \tag{2.24}$$

11

Now the conservation of angular momentum can be used in order to calculate the torque, Q, since it will be equal to the change in angular momentum of the wake, in incremental form (Equation 2.25)

$$dQ = d\dot{m}(wr)r = (\rho U_2 2\pi r dr)(\omega r)r \tag{2.25}$$

And substituting $U_2 = U(1 - a)$ and $a' = \omega/2\Omega$:

$$dQ = 4a'(1 - a)\rho U\Omega\pi r^3 dr \tag{2.26}$$

And the power generated (in incremental form again), dP:

$$dP = \Omega dQ \tag{2.27}$$

Now one can substitute dQ, and bearing in mind $U_2 = U(1 - a)$, $a' = \omega/2\Omega$ and the definition of λ_r, the rearranged equation is given by:

$$dP = \frac{1}{2}\rho AU^3 \left[\frac{8}{\lambda^2}a'(1 - a)\lambda_r^3 d\lambda_r\right] \tag{2.28}$$

In Equation 2.28, the axial and angular induction factors represent the magnitude and direction of the flow.

Now the incremental power coefficient can be expressed as:

$$dC_P = \frac{dP}{\frac{1}{2}\rho AU^3} \tag{2.29}$$

And therefore the integral expression for the power coefficient is:

$$C_P = \frac{8}{\lambda^2} \int_0^\lambda a'(1-a)\lambda_r^3 d\lambda_r \tag{2.30}$$

Now the relation between a, a' and λ_r will give the aerodynamic conditions in order to generate the maximum possible power. This is done by substituting all the relations in the expression $a'(1-a)$ (from Equation 2.35 is seen that this term maximizes the power generation) and setting the derivative with respect to a equal to zero. Using Equation 2.22:

$$a' = -\frac{1}{2} + \frac{1}{2}\sqrt{1 + \frac{4}{\lambda_r a(1-a)}} \tag{2.31}$$

$$\frac{d(a'(1-a))}{da} = 0$$

$$\lambda_r^2 = \frac{(1-a)(-1+4a)^2}{1-3a} \tag{2.32}$$

This local tip ratio will maximize C_p, so substituting it in Equation 2.22:

$$a' = \frac{1-3a}{-1+4a} \tag{2.33}$$

Equation 2.33 defines the angular induction factor for maximum power in each angular ring. Moreover, a relationship between the gradients of a and λ_r (da and $d\lambda_r$), which is given by Equation 2.32:

$$2\lambda_r d\lambda_r = \frac{6(-1+4a)(1-2a)^2}{(1-3a)^2}da \tag{2.34}$$

Then the power coefficient expression for maximizing the output in integral form (from Equation 2.35) can be rewritten as:

13

$$C_{P,max} = \frac{24}{\lambda^2} \int_{a_1}^{a_2} [\frac{(1-a)(1-2a)(1-4a)}{(1-3a)}]^2 da \qquad (2.35)$$

For the limits of the integral, a_1 corresponds to $\lambda_r = 0$ and a_2 to $\lambda_r = \lambda$. Making use of Equation 2.32 for λ the value $a_1 = 0.25$ is calculated as the lower limit, and the upper limit (a_2) corresponds to operation at tip speed ratios of interest. Here each tip speed ratio will have a correspondent a_2 until it gets to $a_2 = 1/3$, which is the limit, since it will correspond to an infinite tip speed ratio. Therefore C_p can be written as a function of λ (a_2 is a function of λ as well). With all this data Figure 2.4 can be calculated in order to plot the results and compare them with the 1-D approach (Betz theoretical limit).
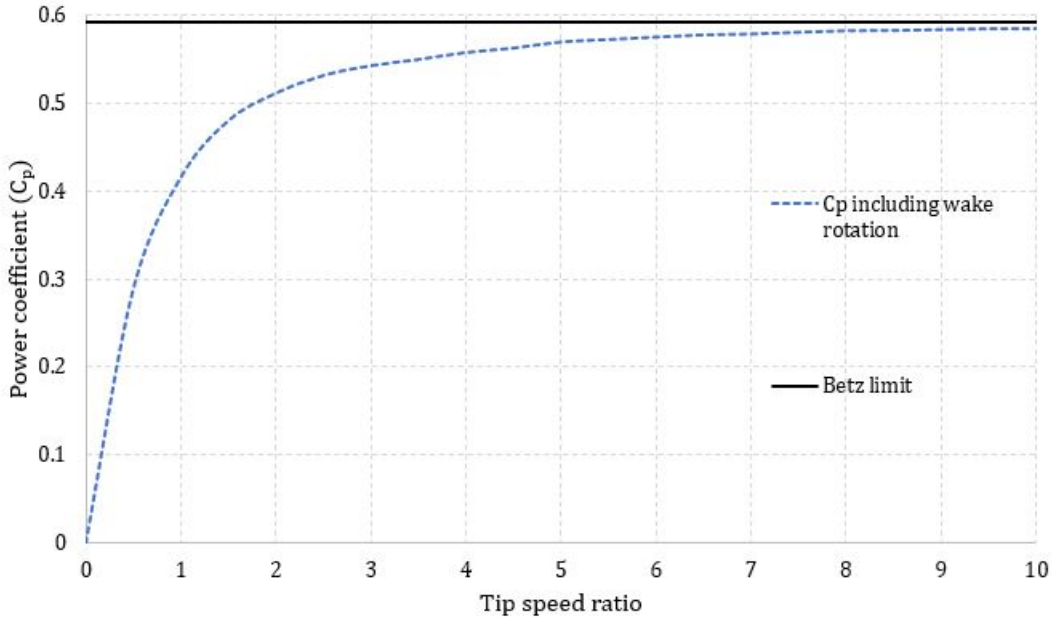
Figure 2.4: Theoretical maximum power coefficient as a function of tip speed ratio for an ideal horizontal axis wind turbine, with and without wake rotation

Figure 2.4 clearly shows how wake rotation heavily affects the efficiency of wind turbines with low rotational speeds in which the torque extracted is higher, as previously said at the beginning of this section. In addition, the higher the tip speed ratio, the closer the power coefficient can approach the theoretical maximum power extraction. It should be mentioned that angular induction factor gets close to zero in the outer parts of the rotor, while increasing exponentially when approaching the hub, which means a high angular velocity of the flow compared to the angular velocity of the rotor (Equation 2.19).

In the previous sections the nature of the air flow around the wind turbine was studied

using physics in order to extract theoretical limits and compare them with a more complex model. In the next sections aerodynamics theory will be used with the purpose of showing how these limits can be achieved optimizing airfoils' design.

2.d   General Concepts of Aerodynamics

Lift generated in a wing (in the case of an airplane), and (in the case of a wind turbine) normal force in the blades so as to produce mechanical power, is made by the relative motion between an airfoil and a surrounding fluid. An airfoil (see Figure 2.5) is the cross-sectional shape of a wing or blade, and produces aerodynamic forces when moving through a fluid. The component of this force perpendicular to the direction of motion is called lift and the component parallel to the direction of motion is called drag. Subsonic flight airfoils have a characteristic shape with a rounded leading edge, followed by a sharp trailing edge, and some times with a symmetric curvature of upper and lower surfaces.
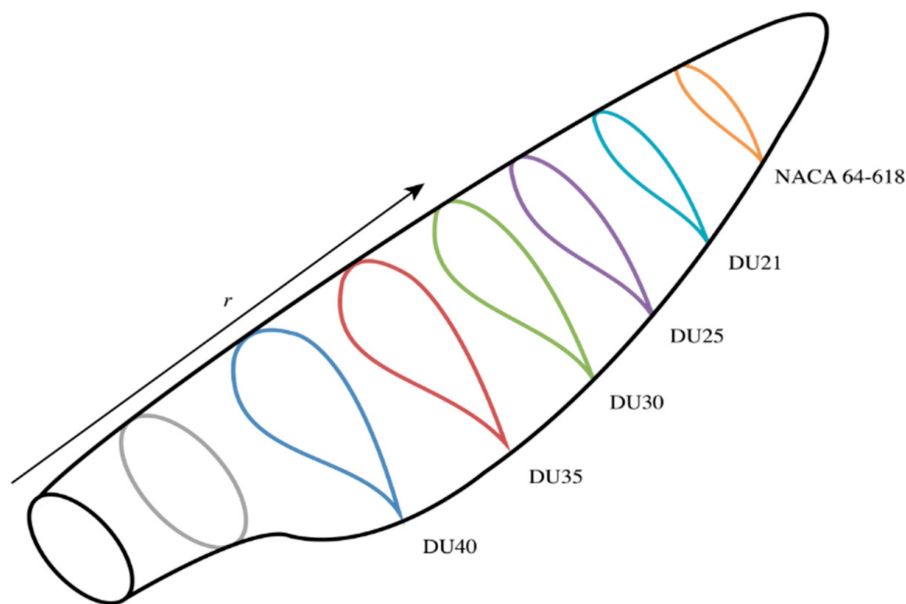
Figure 2.5: Wind turbine blade with its different airfoils (designated in different nomenclatures) depending on the section

The width and length of the blade are functions of the desired aerodynamic performance, the maximum desired rotor power, the assumed airfoil properties, and strength considerations. Before the details of wind turbine power production are explained, aerodynamic concepts related to airfoils need to be discussed.

2.d.i   Lift, Drag, Moment and Non-dimensional Parameters

As previously mentioned, an airfoil produces aerodynamic forces over its surface. This is due to the fact that fluids accelerate in convex surfaces, decreasing the pressure on that side of the airfoil, and thus creating a 'suction' effect, since the other side (with more pressure) is 'pushing' in the direction of the 'suction side' and therefore generating lift. In addition, viscous friction slows down the flow near the surface, which has some effects on the forces as well.
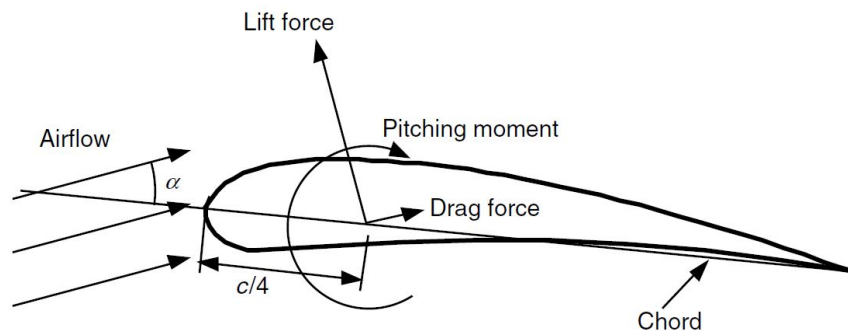
Figure 2.6: Forces and moments on an airfoil section. The direction of positive forces and moments is indicated by the direction of the arrow

As can be seen in Figure 2.6, the resultant forces and viscous effects can be resolved into lift, drag and pitching moment, which can also be simplified and assumed that their resultants are applied at a distance of $c/4$ from the leading edge.

Moreover, non-dimensional parameters are used to describe the flow characteristics, being the Reynolds number the most important one, since it relates the convective or inertial forces to the viscous ones, and giving an idea of the regime (laminar or turbulent) of the flow with respect to the shape of the body:

$$Re = \frac{Ul}{v} = \frac{\rho Ul}{\mu} = \frac{Inertial\ force}{Viscous\ force} \tag{2.36}$$

where ρ is the fluid density, μ is fluid viscosity, $v = \mu/\rho$ is the kinematic viscosity, and U and l are a velocity and length that characterize the scale of the flow. At low Reynolds numbers, flows tend to be dominated by laminar (sheet-like) flow, while at high Reynolds numbers flows tend to be turbulent. The turbulence results from differences in the fluid's speed and direction, which may sometimes intersect or even move counter to the overall direction of the flow (eddy currents).

In addition, other non-dimensionalized coefficients need to be defined: two-dimensional lift,

16

drag, pitching moment and pressure coefficients (respectively Equations 2.37, 2.38, 2.39 and 2.41). These are calculated (with the help of wind tunnel tests for computing the forces) as follows:

$$C_l = \frac{\frac{L}{l}}{\frac{1}{2}\rho U^2 c} = \frac{Lift\, force/unit\, length}{Dynamic\, force/unit\, length} \tag{2.37}$$

$$C_d = \frac{\frac{D}{l}}{\frac{1}{2}\rho U^2 c} = \frac{Drag\, force/unit\, length}{Dynamic\, force/unit\, length} \tag{2.38}$$

$$C_m = \frac{M}{\frac{1}{2}\rho U^2 A c} = \frac{M}{\frac{1}{2}\rho U^2 l c^2} = \frac{Pitching\, moment}{Dynamic\, moment} \tag{2.39}$$

$$C_p = \frac{p - p_\infty}{\frac{1}{2}\rho U^2} = \frac{Static\, pressure}{Dynamic\, pressure} \tag{2.40}$$

where A is the projected airfoil area ($A = cl$), p the pressure at some point of the airfoil and p_∞ the incoming air pressure.

All these coefficients, as well as the surface roughness ratio (ε/l=Surface roughness height/unit length), will be used to analyze airfoil flow along the section.

For three-dimensional objects (C_L, C_D and C_M), additional wind tunnel tests will be needed, since 3D blades have a finite span and force and moment coefficients are affected by the flow around the end of the airfoil. Two-dimensional airfoil data, on the other hand, are assumed to have an infinite span (no end effects).

2.d.ii   Flow Around an Airfoil and its Behaviour

As seen in previous sections, lift, drag and pitching moment are caused due to pressure changes, which can be explained by changes in air velocity. These two phenomena are related in the Bernoulli's principle, which for non-viscous flows can be stated as:

$$p + \frac{1}{2}\rho U^2 = Static\, pressure + Dynamic\, pressure = constant \tag{2.41}$$

One can see that if the flow accelerates through the surface (p.e upper side of an airfoil), pressure will drop, creating a negative pressure gradient, and vice versa, for example when the flow decelerates in the trailing edge, the surface pressure increases and a positive pressure gradient is created. In order to calculate the behaviour of an airfoil, the integral of all its points on the upper surface must be computed, and then the lift and pitching moment can be calculated bearing in mind the pressure distribution.

In the case of drag, in addition to the pressure distribution over the airfoil, viscous effects between the air flow and the surface play a major role. This friction produces two different regions: the boundary layer, next to the surface, where viscous effects predominate and another region further from the airfoil surface, where frictional effects are negligible.
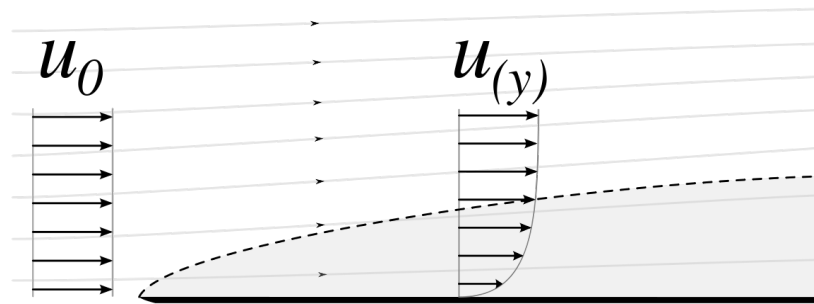
Figure 2.7: Boundary layer representation

Boundary layer thickness in a turbine blade may vary from one millimeter to several tens of centimeters depending on the size of the wind turbine, the flow conditions and the surface roughness. In the boundary layer, the velocity of the flow increases from zero at the surface to the velocity of the flow outside the boundary layer (velocity in the boundary layer is a function of distance to the surface). Depending on the viscosity and the inertial forces, the boundary layer might display laminar (smooth and steady) or turbulent (irregular with vortices) flow. Usually from the leading edge of an airfoil up to some point near the trailing edge the flow remains laminar, however, due to the interaction of the viscous and inertial forces, this flow turns into a turbulent one, more chaotic (right part of increasing pressure gradient of Figure 2.8), where frictional forces are way higher than in the laminar zone of the boundary layer .
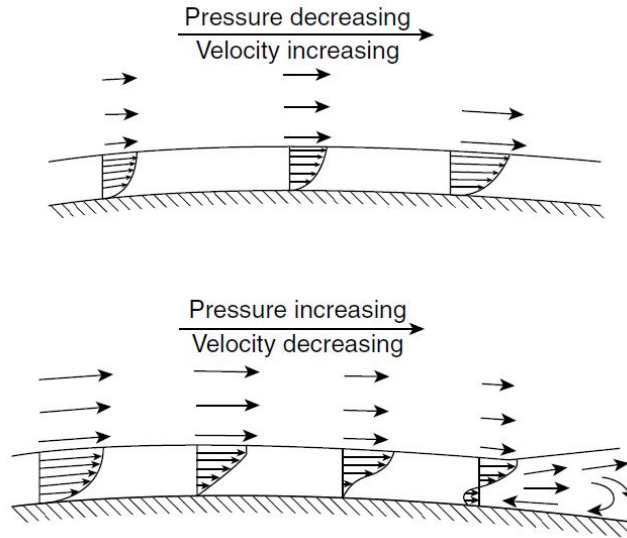
Figure 2.8: Effects of favorable (decreasing) and adverse (increasing) pressure gradients on the boundary layer

As Figure 2.8 shows, flow in the boundary layer is accelerated or decelerated depending on the pressure gradient, while is always decelerated by friction in the surface. The combination of a negative pressure gradient and friction might cause the flow to stop or even go in the reverse direction, which results in a flow separation from the surface, and therefore losing lift, since an airfoil can only efficiently produce lift as long as the surface pressure distributions can be supported by the boundary layer.

This turbulence in the boundary layer must not be confused with the atmosphere one, as a wind turbine will produce a much larger turbulence with its wake, while he boundary layer is only sensitive to fluctuations on the order of the size of the boundary layer itself. Thus, the atmospheric turbulence does not affect the airfoil boundary layer directly. It may affect it indirectly through changing angles of attack, which will change the flow patterns and pressure distributions over the blade surface.

The flow behaviour can be understood with the help of streamlines, which can be thought of as the path that a particle would take if placed in a flowing fluid. In Figure 2.9 one can see how by increasing the angle of attack the flow is finally detached (last picture), entering stall conditions and losing most of the airfoil efficiency. On the other hand, in the first picture, streamlines which converge indicate an increase in velocity and a decrease in pressure (and the opposite for diverging streamlines). In these cases the Bernoulli's equation can be applied for each streamline in different places along the chord.
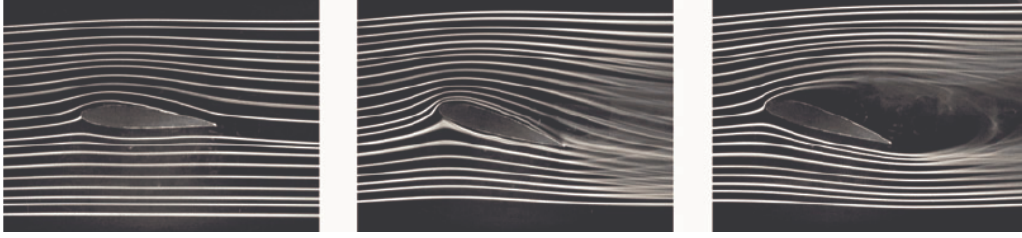
Figure 2.9: Streamlines around an airfoil at increasing angles of attack

Turbulent flow is characterized by its vorticity (ζ), that describes the flow rotational velocity, and circulation (Γ), which is the integral of the vorticity of each element multiplied by their incremental areas and describes the flow rotational behaviour along the span of the blade.

$$\zeta = \frac{\partial u}{\partial y} - \frac{\partial v}{\partial x} \tag{2.42}$$

$$\Gamma = \int \int (\frac{\partial u}{\partial y} - \frac{\partial v}{\partial x}) dx dy \tag{2.43}$$

where u is the velocity component in the direction of the flow (x) and v is the component perpendicular to the flow (y).

Lift per unit span ($L' = L/l$) is given by the expression $L' = \rho U_\infty \Gamma$, being U_∞ the free stream velocity. Using the shape of a cylinder of radius r as a first calculation, its maximum circulation value is $\Gamma = 4\pi U_\infty r$, yielding a lift coefficient (Cl) of 4π, which can be transformed into an airfoil making a change of variable of coordinates and simplifying the calculus.

This method of analysis (the application of transformations of shapes, streamlines, and pressure distributions) provides the foundation of thin airfoil theory, which is used to predict the characteristics of most commonly used airfoils. Thin airfoil theory shows, that the lift coefficient of a symmetrical airfoil at low angles of attack is equal to $2\pi\alpha$ (when the angle a is measured in radians), as can be seen in Figure 2.10. Nevertheless for higher angles of attack this assumption is no longer valid, but more detail on the theory of lift and circulation, as well as on the use of transformations can be found in literature such as *Fundamental of Aerodynamics* [8].
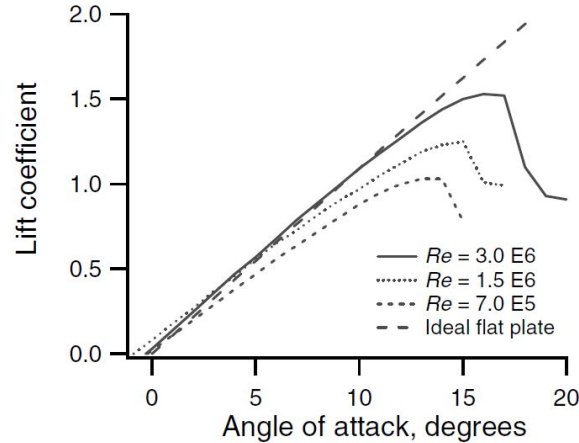
Figure 2.10: Lift and drag coefficients for the NACA 0012 symmetric airfoil (Re, Reynolds number)

Airfoils for horizontal axis wind turbines (HAWTs) are cambered (not symmetric, asymmetric between the two acting surfaces of the airfoil, with the top surface of a wing commonly being more convex) and designed to be used at low angles of attack, where lift coefficients are fairly high and drag coefficients are fairly low. The drag coefficient is usually much lower than the lift coefficient at low angles of attack and it increases at higher angles of attack. Moreover, the behaviour of the airfoil is affected by the Reynolds number: as Reynolds numbers decrease, viscous forces get more important compared to inertial forces, which increases the effects of surface friction, decreasing velocities, increasing the pressure gradient, and therefore decreasing the lift generated by the airfoil.

Due to the different conditions in which an airfoil can operate, David A. Spera [9] sorted three types of flow regime: the attached flow regime, the high lift/stall development regime, and the flat plate/fully stalled regime.

- **Attached Flow Regime**. At low angles of attack (up to about 7 degrees for cambered airfoils), the flow is attached to the upper surface of the airfoil. In this attached flow regime, lift increases with the angle of attack and drag is relatively low.

- **High Lift/Stall Development Regime**. In the high lift/stall development regime (from about 7 to 11 degrees), the lift coefficient peaks as the airfoil becomes increasingly stalled. Stall occurs when the angle of attack exceeds a certain critical value (10 to 16 degrees, depending on the Reynolds number) and separation of the boundary layer on the upper surface takes place, as shown in the right image of Figure 2.9. This causes a wake to form above the airfoil, which reduces lift and increases drag.

- **Flat Plate/Fully Stalled Regime**. In the flat plate/fully stalled regime, at larger angles of attack up to 90 degrees, the airfoil acts increasingly like a simple flat plate with approximately equal lift and drag coefficients at an angle of attack of 45 degrees and zero lift at 90 degrees.

21

3   Blade Design for Modern Wind Turbines

Generally, in the 1970s and early 1980s, wind turbine designers felt that minor differences in airfoil performance characteristics were far less important than optimizing blade twist and taper (relation between the chord at the tip and at the root). For this reason, little attention was paid to the task of airfoil selection. Thus, airfoils that were in use by the aircraft industry were chosen because aircraft were viewed as similar applications. Aviation airfoils such as the NACA 44xx and NACA 230xx were popular airfoil choices because they had high maximum lift coefficients, low pitching moment, and low minimum drag.

The NACA classification has 4, 5, and 6 digit series wing sections. For wind turbines, four-digit series were generally used, for example NACA 4415 (Figure 3.1). The first integer indicates the maximum value of the mean camber line ordinate in percent of the chord. The second integer indicates the distance from the leading edge to the maximum camber in tenths of the chord. The last two integers indicate the maximum section thickness in percent of the chord.
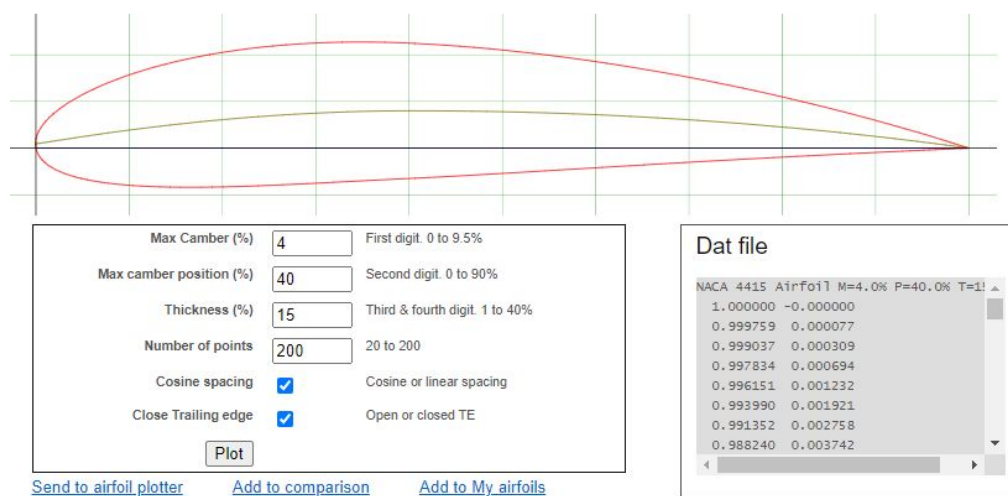
Figure 3.1: NACA 4415 airfoil in a 4 digit airfoil generator (`http://airfoiltools.com/airfoil/naca4digit`)

In the 1980s, there were some advances regarding the leading edge roughness, nevertheless, stall-controlled HAWTs commonly produced too much power in high winds, causing generator damages, and that was the reason why these turbines operated half of its useful life with most part of its blades in stall conditions. Predicted loads were only 50% to 70% of the measured loads. Designers began to realize that a better understanding of airfoil stall performance was important. In addition, leading edge roughness affected rotor performance. For example, with the early airfoil designs, when the blades accumulated insects and dirt along the leading edge, power output could drop as much as 40% of its clean value. Moreover, pitch-controlled wind turbines (the blades are rotate along their axis to control loads), often experienced excessive

loads or load fluctuations during gusts, before the pitch system could rotate the blade, entering stall conditions before the pitch system actuated.

As a consequence of these experiences, airfoil selection criteria and the designs for wind turbine airfoils and blades have had to change to achieve high and reliable performance. Nowadays engineers design airfoils specifically for HAWTs, using mainly the code developed by Eppler and Somers (1980), and others like XFOIL, RFOIL and PROFOIL. These codes combine a variety of techniques to optimize boundary layer characteristics and airfoil shapes to achieve specified performance criteria.

The National Renewable Energy Laboratory developed special purpose families of airfoils for three different classes of wind turbine using the Eppler code, and the same in Europe (researchers of the Delft University of Technology) using the XFOIL and RFOIL codes during 1990s. In Delft they also focused on achieving low sensitivity to surface roughness, and they did it by locating the point of transition to turbulent flow near the leading edge, as the flow approached stall. DUT also designed airfoils for the blade tips of pitch-controlled rotors with the design lift coefficient (the lift coefficient at the maximum lift–drag ratio) close enough to the peak lift coefficient to minimize changes in lift and, thus, peak loads as gusts occurred, but with a design angle of attack far enough from stall to minimize the fluctuating loads from stall before the pitch system could react.

Larger wind turbines that were built in the later 1990s required even thicker airfoils for structural strength. To deliver sufficient torque at low wind speeds, without significantly large chords, the maximum lift coefficients need to be high on these inboard airfoils. Some compromises needed to be made, as high maximum lift coefficients often accompany sensitivity to leading edge roughness. An additional complication is that the inner portion of the blade is more subject to flow distortions due to the rotation of the blades. The Delft University of Technology addressed these issues by using an updated version of XFOIL (RFOIL) to design a number of thick airfoils for wind turbines that met their design criteria while operating in the flow field in the inner portion of the blade. All these studies can be seen in detail in the *Summary of the Delft University Wind Turbine Dedicated Airfoils* [10].

For the design of the different airfoil shapes along the blades, one should take into account the variation of flow conditions, and choose a performance in a range of situations that will determine the choice of airfoil, chord length and twist along the blade. This choice has changed over the years, as explained previously, until nowadays, when rotors are designed for minimum cost of energy. This approach also starts with a rotor that is as aerodynamically efficient as possible. The rotor design is then optimized using a multidisciplinary approach that includes wind characteristics, an aerodynamic model, a structural model of the blades, and cost models for the blades and all major wind turbine components. Such approaches have resulted in slightly lower energy capture than previous designs, but lower loads (by about 10%) and lower

overall cost of energy.

These designs are achieved thanks to computer codes that model not only the aerodynamics of the rotor, but also the motions of the elastically deforming blades and the interactions between these blade motions and the flow, so they are usually called aeroelastic codes. These codes can calculate the interaction between the boundary layers around the airfoil, the production of power and the flow field around the wind turbine, and then manufacturers use these results to improve the performance of their wind turbines and to get their wind turbine design certified according to international standards.

The aeroelastic codes are based on blade element momentum (BEM) theory, which describes the steady state behavior of a wind turbine rotor, with extensions to address unsteady operation. Section 3.a will describe this type of analysis. More complicated modeling tools that are being developed to more accurately model the rotor aerodynamics will be also explained (taking into account the effect of drag, wake rotation and number of blades) in Section 3.c.iii.

In this section, in addition to the BEM theory explanation, a simple (infinite blades and no wake) optimum blade design will be presented, as well as another optimum design including wake rotation and a finite number of blades, which can be used as a first approach for a real design. Along the analysis and calculation, performance characteristics like forces, power coefficients and air flow characteristics will be compared between the different approaches.

3.a   Momentum and Blade Element Theory

As already presented in previous sections, a wind turbine generates lift thanks to a pressure difference across its airfoils, producing a pressure change like the one caused by the actuator disk seen in Section 2.b. For the calculation of the flow field around a wind turbine rotor by the actuator disk the conservation of linear and angular momentum was used, and the axial and angular induction factors (function of the rotor power extraction and thrust) were presented in order to characterize this flow field.

For the analysis shown here, momentum theory and blade element theory will be assessed. Momentum theory refers to a control volume analysis of the forces at the blade based on the conservation of linear and angular momentum. Blade element theory refers to an analysis of forces at a section of the blade, as a function of blade geometry. The combination of both analysis is the blade element momentum (BEM) theory, which can be used to relate blade shape to the rotor's ability to extract power from the wind.

3.a.i Momentum Theory

Force is the rate of change of momentum, and considering conservation of linear and angular momentum, all necessary equations have already been developed in Section 2.c, yielding:

$$dT = 4a(1-a)\rho U^2 \pi r dr \tag{3.1}$$

$$dQ = 4a'(1-a)\rho U \Omega \pi r^3 dr \tag{3.2}$$

Thus, from momentum theory one gets two equations, Equations 3.1 and 3.2, that define the thrust and torque on an annular section of the rotor as a function of the axial and angular induction factors.

3.a.ii Blade Element Theory

One can also use the angle of attack and lift and drag coefficients in order to express the forces on the blade of a wind turbine. For the explanation, no radial flow will be taken into account, nor other forces apart from the lift and drag characteristics of the airfoil shape of the blades.
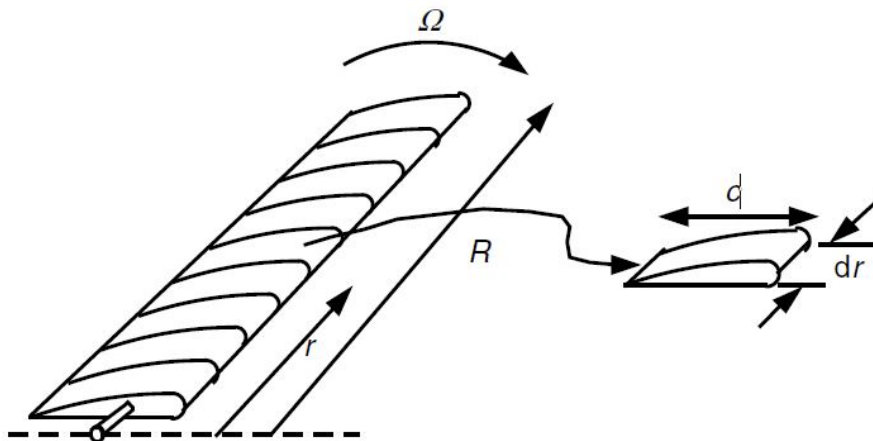
Figure 3.2: Schematic of blade elements; c, airfoil chord length; dr, radial length of element; r, radius; R, rotor radius; Ω, angular velocity of rotor
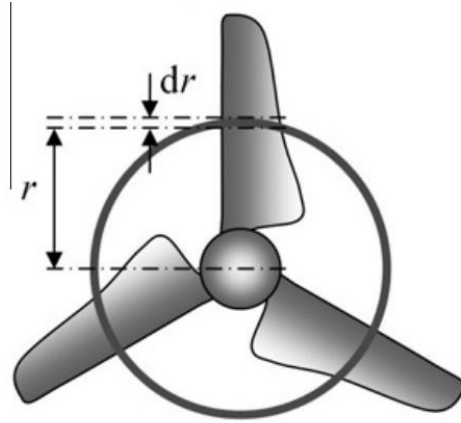
Figure 3.3: Schematic of discretization of the rotor

In analyzing the forces on the blade section, it must noted that the lift and drag forces are perpendicular and parallel, respectively, to an effective, or relative, wind (see Figure 3.4). The relative wind is the vector sum of the wind velocity at the rotor, $U(1 - a)$, and the wind velocity due to rotation of the blade. This rotational component is the vector sum of the blade section velocity, Ωr, and the induced angular velocity at the blades from conservation of angular momentum, $\omega r/2$, or

$$\Omega r + \omega r/2 = \Omega r + \Omega a'r = \Omega r(1 + a') \tag{3.3}$$
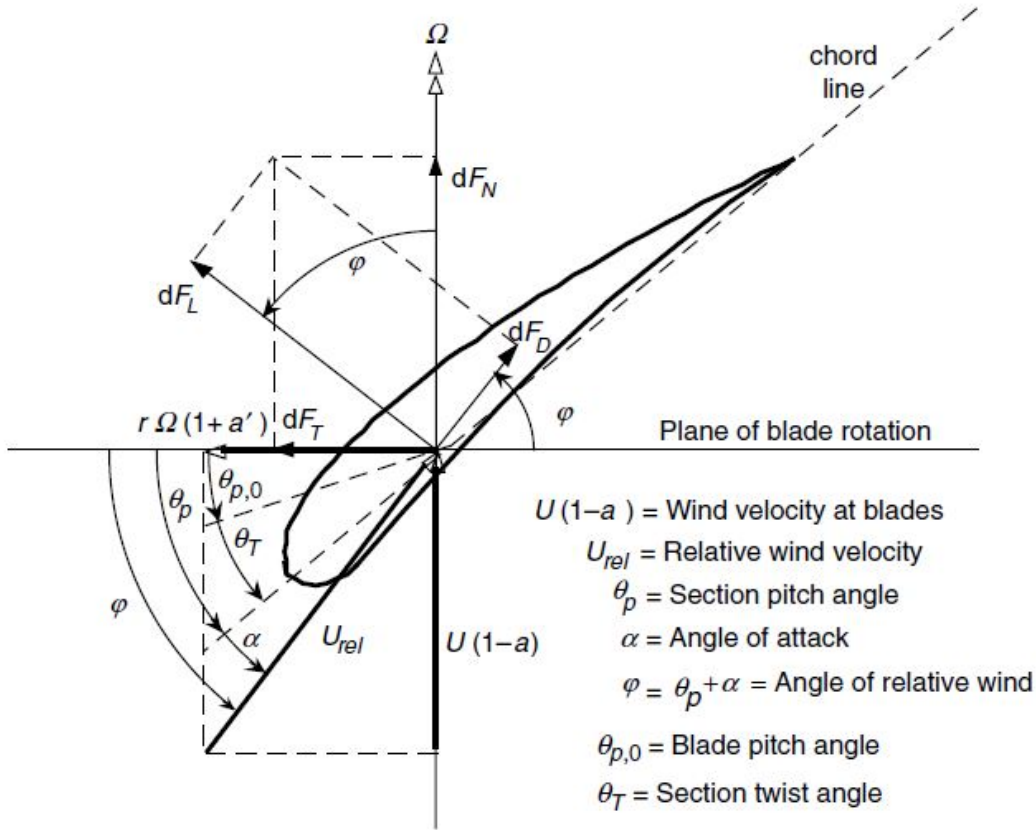
Figure 3.4: Blade geometry for analysis of a horizontal axis wind turbine

Here, θ_p is the section pitch angle, which is the angle between the chord line and the plane of rotation; $\theta_{p,0}$ is the blade pitch angle at the tip; θ_T is the blade twist angle; α is the angle of attack (the angle between the chord line and the relative wind); φ is the angle of relative wind; dF_L is the incremental lift force; dF_D is the incremental drag force; dF_N is the incremental force normal to the plane of rotation (this contributes to thrust); and dF_T is the incremental force tangential to the circle swept by the rotor. This is the force creating useful torque. Finally, U_{rel} is the relative wind velocity.

Note from Figure 3.4 that θ_T can be written as $\theta_T = \theta_p - \theta_{p,0}$. Moreover, the angle of the relative wind is the sum of the section pitch angle and the angle of attack ($\varphi = \theta_p + \alpha$). In addition the twist angle is, of course, a function of the blade geometry, whereas θ_p changes if the position of the blade, $\theta_{p,0}$, is changed.

Now one can make the follow relations with the help of Figure 3.4:

$$tan\varphi = \frac{U(1-a)}{\Omega r(1+a')} = \frac{1-a}{(1+a')\lambda_r} \qquad (3.4)$$

$$U_{rel} = U(1 - a)/sin\varphi \tag{3.5}$$

$$dF_L = C_l\frac{1}{2}\rho U_{rel}^2 cdr \tag{3.6}$$

$$dF_D = C_d\frac{1}{2}\rho U_{rel}^2 cdr \tag{3.7}$$

$$dF_N = dF_L cos\varphi + dF_D sin\varphi \tag{3.8}$$

$$dF_T = dF_L sin\varphi - dF_D cos\varphi \tag{3.9}$$

If the rotor has B blades, the total normal force on the section at a distance, r, from the center is:

$$dF_N = B\frac{1}{2}\rho U_{rel}^2(C_l cos\varphi + C_d sin\varphi)cdr \tag{3.10}$$

And the differential torque due to the tangential force operating at a distance, r, from the center is given by:

$$dQ = BrdF_T = B\frac{1}{2}\rho U_{rel}^2(C_l sin\varphi - C_d cos\varphi)crdr \tag{3.11}$$

So now another two equations for the normal force (thrust) and tangential force (torque) on the annular rotor section are defined (Equations 3.10 and 3.11 respectively). They are a function of the flow angles and airfoil characteristics. Note that drag is decreasing torque (and

28

therefore power), however is increasing the thrust. In the following sections, several assumptions will be taken to determine ideal blade shapes for optimum performance and to determine rotor performance for any arbitrary blade shape.

3.b   Blade Shape for Ideal Rotor without Wake Rotation

Here a simple example will be presented so that the method to follow to get a first blade design is clear. In this analysis no wake rotation will be used ($a' = 0$), as well as no drag ($C_d = 0$ and an infinite number of blades. The axial induction factor, a, is assumed to be the optimum 1/3 (as seen in Section 2.b).

The next step would be to choose an appropriate tip speed ratio (λ), number of blades (B), radius (R) and an airfoil with known lift and drag coefficients as a function of angle of attack. This angle of attack should be selected where C_d/C_l is minimal in order to most closely approximate the assumption that drag is 0.

From momentum theory (Equation 3.1) and the assumption of $a = 1/3$, one can get:

$$dT = \frac{8}{9}\rho U^2 \pi r dr \tag{3.12}$$

and from blade element theory (Equation 3.10), assuming $C_d = 0$:

$$dF_N = B\frac{1}{2}\rho U_{rel}^2 (C_l cos\varphi)cdr \tag{3.13}$$

Finally a two more equations from blade element theory will be simplified using the assumptions made:

$$U_{rel} = U(1-a)/sin(\varphi) = \frac{2U}{3sin(\varphi)} \tag{3.14}$$

$$tan\varphi = \frac{1-a}{(1+a')\lambda_r} = \frac{2}{3\lambda_r} = \frac{2}{3\lambda\, r/R} \tag{3.15}$$

Combining Equations 3.12, 3.13, 3.14 and 3.15 (since dT would be equal to dF_N) yields the following equation:

$$\frac{C_l B c}{4\pi r} = tan(\varphi)sin(\varphi) = \frac{2}{3\lambda\, r/R}sin(\varphi) \qquad (3.16)$$

From where the chord c can be extracted:

$$c = \frac{8\pi r sin(\varphi)}{3BC_l\lambda\, r/R} \qquad (3.17)$$

And the chord and radius (r) can be non-dimensionalized by dividing by the rotor radius. Giving some values for the example, like $\lambda = 8$, $C_l = 1$, $\alpha = 6$ (for this value C_d/C_l is minimum) and a wind turbine with three blades ($B = 3$), one can calculate the non-dimensional chord of the blades, angles and relate them with the help of Figure 3.4 relations (explained in the paragraphs under the image).

The example has been calculated, giving the following results:

r/R	c/R	Twist angle $(\theta_T)(deg)$	Angle of rel. wind $(\varphi)(deg)$	Section pitch angle $(\theta_p)(deg)$
0.1	0.22	35.04	39.81	33.81
0.2	0.13	17.86	22.62	16.62
0.3	0.09	10.76	15.52	9.52
0.4	0.07	7.00	11.77	5.77
0.5	0.06	4.70	9.46	3.46
0.6	0.05	3.14	7.91	1.91
0.7	0.04	2.03	6.79	0.79
0.8	0.04	1.18	5.95	-0.05
0.9	0.03	0.53	5.29	-0.71
1	0.03	0	4.76	-1.24

Table 1: Twist and chord distribution for the example Betz optimum blade; r/R, fraction of rotor radius; c/R, non-dimensionalized chord
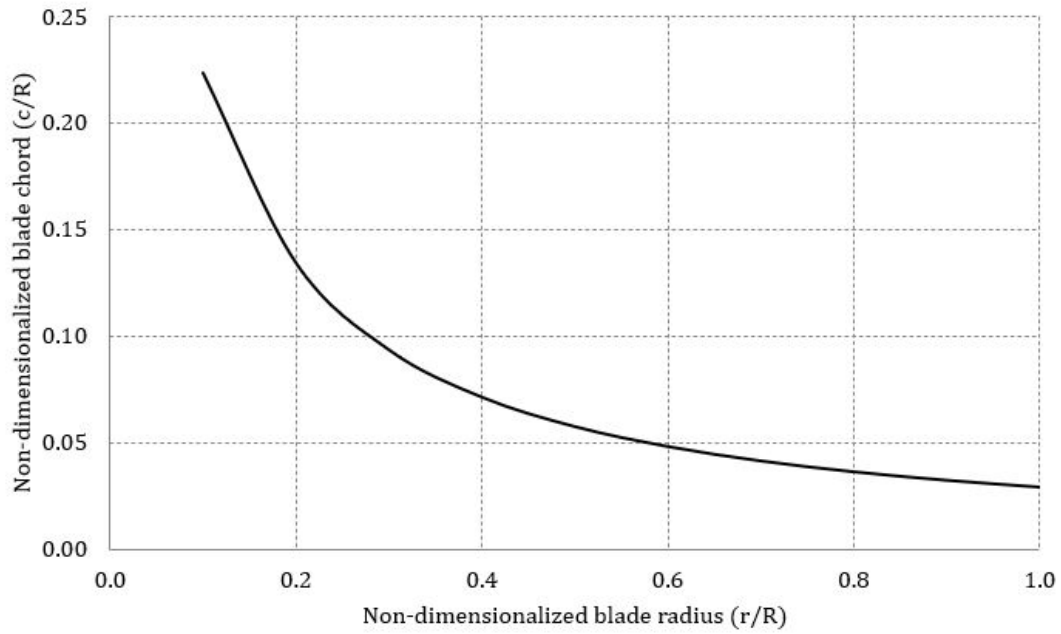
Figure 3.5: Blade chord for the example
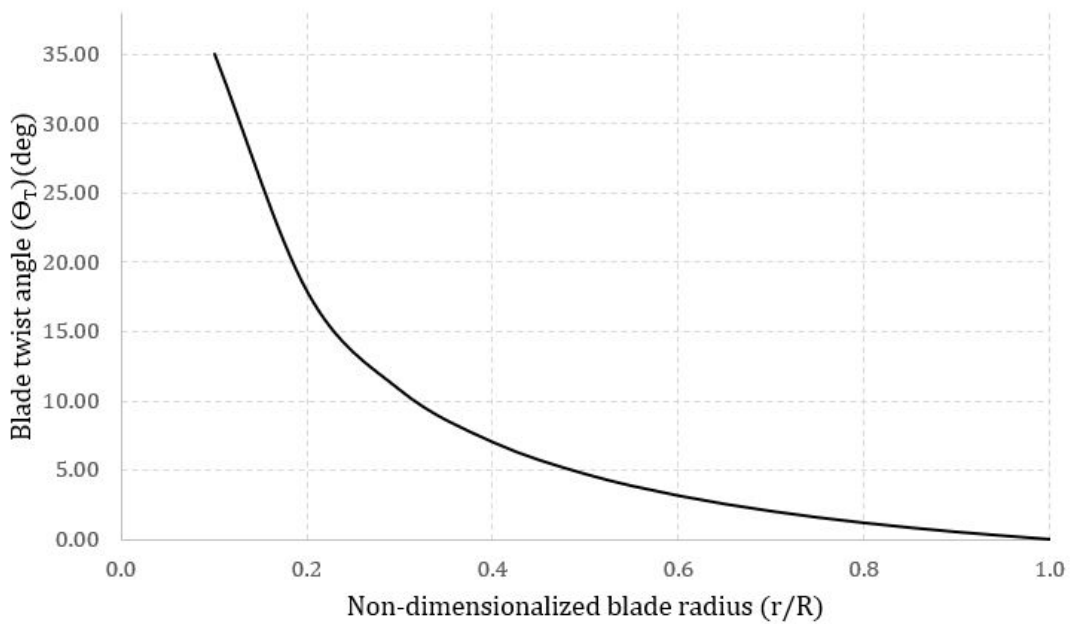
Figure 3.6: Blade twist angle for sample

It can be seen that blades designed for optimum power production have an increasingly large chord and twist angle as it gets closer to the blade root, characteristics that could make fabrication more laborious, since another consideration in blade design is the cost and difficulty of fabricating the blade. An optimum blade would be very difficult to manufacture at a reasonable cost, but the design provides insight into the blade shape that might be desired for a wind turbine.

In general, a rotor is not of the optimum shape because of fabrication difficulties. Furthermore, when an 'optimum' blade is run at a different tip speed ratio than the one for which it is designed, it is no longer 'optimum'. Thus, blade shapes must be designed for easy fabrication and for overall performance over the range of wind and rotor speeds that they will encounter. In considering non-optimum blades, one generally uses an iterative approach. That is, one can assume a blade shape and predict its performance, try another shape and repeat the prediction until a suitable blade has been chosen.

3.c   Real Blade Performance Prediction

In previous sections, the blade shape for an ideal rotor without wake rotation has been considered. In this section, the analysis of arbitrary blade shapes is considered. This analysis includes wake rotation, drag, losses due to a finite number of blades, and off-design performance.

3.c.i   Blade Performance Including Wake Rotation

Here, the already known four equations (3.1, 3.2, 3.10 and 3.11) derived from momentum and blade elements theory will be used. From momentum theory:

$$dT = 4a(1-a)\rho U^2 \pi r dr$$

$$dQ = 4a'(1-a)\rho U \Omega \pi r^3 dr$$

and blade element theory:

$$dF_N = B\tfrac{1}{2}\rho U_{rel}^2(C_l cos\varphi + C_d sin\varphi)cdr$$

$$dQ = B\tfrac{1}{2}\rho U_{rel}^2(C_l sin\varphi - C_d cos\varphi)crdr$$

which can be both rewritten using the relation between U_{rel} and U (Equation 3.5):

$$dF_N = \sigma'\pi\rho\frac{U^2(1-a)^2}{sin^2(\varphi)}(C_l cos\varphi + C_d sin\varphi)rdr \tag{3.18}$$

$$dQ = \sigma'\pi\rho\frac{U^2(1-a)^2}{sin^2(\varphi)}(C_l sin\varphi - C_d cos\varphi)r^2 dr \tag{3.19}$$

32

where σ' is the local solidity of an airfoil located at a distance r from the hub:

$$\sigma' = \frac{Bc}{2\pi r} \tag{3.20}$$

The manufacturing of the resulting blade turbine should be as simple as possible. In this sense, the maximum local solidity should never exceed from certain value. If this solidity is too high it will be difficult to construct the transition between it and the hub.

For the next step, the accepted practice is to assume $C_d = 0$, since for airfoils with low drag coefficients this simplification yields negligible errors. By equation Equations 3.1 and 3.18 (normal forces from momentum and blade element theory) and applying the drag simplification one gets:

$$\frac{a}{(1-a)} = \sigma' C_l \frac{cos(\varphi)}{4sin^2(\varphi)} \tag{3.21}$$

and using the same procedure for the torque equations (Equations 3.2 and 3.19):

$$\frac{a'}{(1-a)} = \frac{\sigma' C_l}{4\lambda_r sin(\varphi)} \tag{3.22}$$

From these two resulting equations (3.21 and 3.22) and introducing Equation 3.4, after some rearranging one can get the following useful relations[5]:

$$C_l = 4sin\varphi \frac{cos\varphi - \lambda_r sin\varphi}{\sigma'(sin\varphi + \lambda_r cos\varphi)} \tag{3.23}$$

$$\frac{a'}{(1+a')} = \frac{\sigma' C_l}{4cos(\varphi)} \tag{3.24}$$

$$\frac{a}{a'} = \frac{\lambda_r}{tan\varphi} \tag{3.25}$$

$$a = \frac{1}{[1 + \frac{4sin^2\varphi}{\sigma' C_l cos\varphi}]} \tag{3.26}$$

$$a' = \frac{1}{[\frac{4cos\varphi}{\sigma' C_l} - 1]} \tag{3.27}$$

Solution Methods

According to Manwell [5], there are two solution methods in order to determine flow conditions and forces at each blade section, which will be explained down below.

- *Method 1 - Solving C_l and α*

  Knowing the blade geometry and blade conditions, Equation 3.23 has two unknowns: C_l and α. To find the values, the empirical C_l vs. α curves for the chosen airfoil are needed, so that one can numerically solve Equation 3.23 or even plot it and graphically solve it finding the point in which both curves match.

- *Method 2 - Iterating a and a'*

  Another solution (especially useful for highly loaded rotor conditions), is to follow the iterative steps:
  1. Guess values of a and a'.
  2. Calculate the angle of the relative wind from Equation 3.4.
  3. Calculate the angle of attack from $\varphi = \alpha + \theta_0$ and then C_l and C_d .
  4. Update a and a' from Equations 3.21 and 3.22 or 3.26 and 3.27.

3.c.ii   Power Coefficient Calculation and Tip Loss Effect on it

There are two mainly extended expressions for the calculus of the power coefficient, the first one, introduced by Wilson and Lissaman [12] in 1974 (Equation 3.28), which is derived from the power contribution from each annulus ($dP = \Omega dQ$) and the relations introduced in the previous sections:

$$C_P = (8/\lambda^2) \int_{\lambda_h}^{\lambda} \lambda_r^3 a'(1 - a)[1 - (C_d/C_l)cot\varphi]d\lambda_r \tag{3.28}$$

The second one was introduced by de Vries [13] in 1979, which derivation is algebraically complex, yielding the following equation:

$$C_P = (8/\lambda^2) \int_{\lambda_h}^{\lambda} \sin^2 \varphi (cos\varphi - \lambda_r sin\varphi)(sin\varphi + \lambda_r cos\varphi)[1 - (C_d/C_l)cot\varphi]\lambda_r^2 d\lambda_r \qquad (3.29)$$

Usually these equations are solved numerically. Note that even though the axial induction factors were determined assuming zero drag, the drag is now included here in the power coefficient calculation.

At the tip of the rotor blade an air flow occurs from the lower side of the airfoil profile to the upper side. This air flow couples with the incoming air flow to the blade. The combined air flow results in a rotor tip efficiency (F).

De Vries [13] also introduced a convenient approach developed by Prandtl for including the tip loss effect in the power coefficient calculation. This method applies a correction factor, F, which is a function of the number of blades, the angle of relative wind, and the position on the blade:

$$F = \frac{2}{\pi}cos^{-1}\left\{exp\left[-\left(\frac{(B/2)[1 - (r/R)]}{(r/R)sin\varphi}\right)\right]\right\} \qquad (3.30)$$

where the inverse cosine is in radians (otherwise the initial $2/\pi$ must be replaced by $1/90$. Here the force reduction due to the tip loss is being calculated at a radius r, and it affects the forces derived from momentum theory, and since F is always between 0 and 1, Equations 3.1 and 3.2 become:

$$dT = 4Fa(1 - a)\rho U^2 \pi r dr \qquad (3.1a)$$

$$dQ = 4Fa'(1 - a)\rho U\Omega\pi r^3 dr \qquad (3.2a)$$

And therefore all the derived equations (3.21 through 3.27) can be rewritten as:

$$\frac{a}{(1-a)} = \sigma' C_l \frac{cos(\varphi)}{4F sin^2(\varphi)} \tag{3.21a}$$

$$\frac{a'}{(1-a)} = \frac{\sigma' C_l}{4F\lambda_r sin(\varphi)} \tag{3.22a}$$

$$C_l = 4F sin\varphi \frac{cos\varphi - \lambda_r sin\varphi}{\sigma'(sin\varphi + \lambda_r cos\varphi)} \tag{3.23a}$$

$$\frac{a'}{(1+a')} = \frac{\sigma' C_l}{4F cos(\varphi)} \tag{3.24a}$$

$$a = \frac{1}{[1 + \frac{4F sin^2\varphi}{\sigma' C_l cos\varphi}]} \tag{3.26a}$$

$$a' = \frac{1}{[\frac{4F cos\varphi}{\sigma' C_l} - 1]} \tag{3.27a}$$

$$U_{rel} = \frac{U(1-a)}{sin\varphi} = \frac{U}{(\sigma' C_l/4F)cot\varphi + sin\varphi} \tag{3.31}$$

And the power coefficients expressions:

$$C_P = (8/\lambda^2) \int_{\lambda_h}^{\lambda} F\lambda_r^3 a'(1-a)[1 - (C_d/C_l)cot\varphi]d\lambda_r \tag{3.28a}$$

$$C_P = (8/\lambda^2) \int_{\lambda_h}^{\lambda} F sin^2 \varphi (cos\varphi - \lambda_r sin\varphi)(sin\varphi + \lambda_r cos\varphi)[1 - (C_d/C_l)cot\varphi]\lambda_r^2 d\lambda_r \tag{3.29a}$$

3.c.iii Effect of Drag and Blade Number on Optimum Performance

Most wind turbines use two or three blades and, in general, most two-bladed wind turbines use a higher tip speed ratio than most three-bladed wind turbines. This fact makes practical difference in the maximum achievable C_p negligible (when no drag effects are assumed), as can be seen in Figure 3.7. However, the relation between the drag coefficient and lift coefficient does play a major role in the maximum C_p, as Figure 3.8. Therefore when designing a 2 or 3-bladed wind turbine, choosing an appropriate airfoil (with high lift to drag ratios).
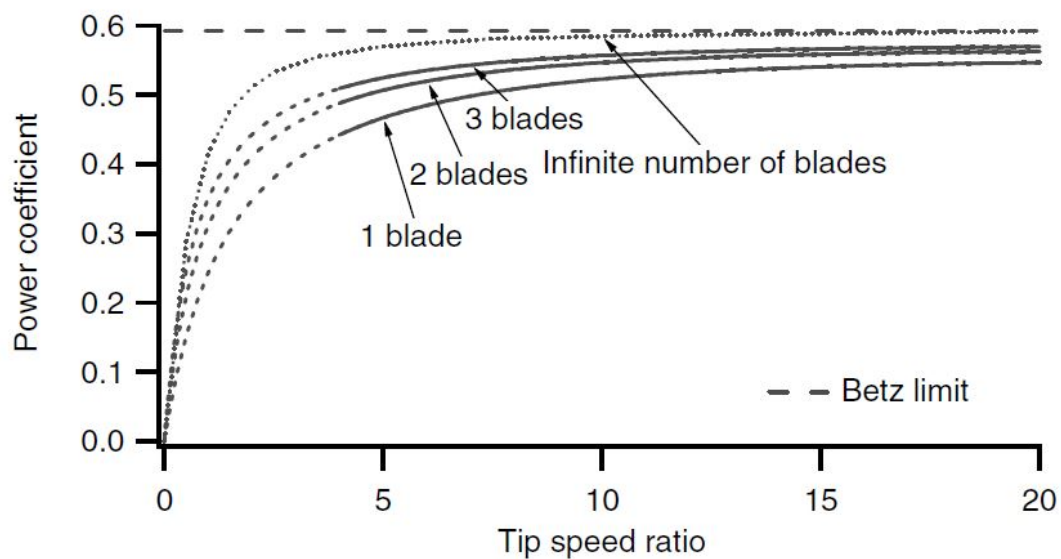
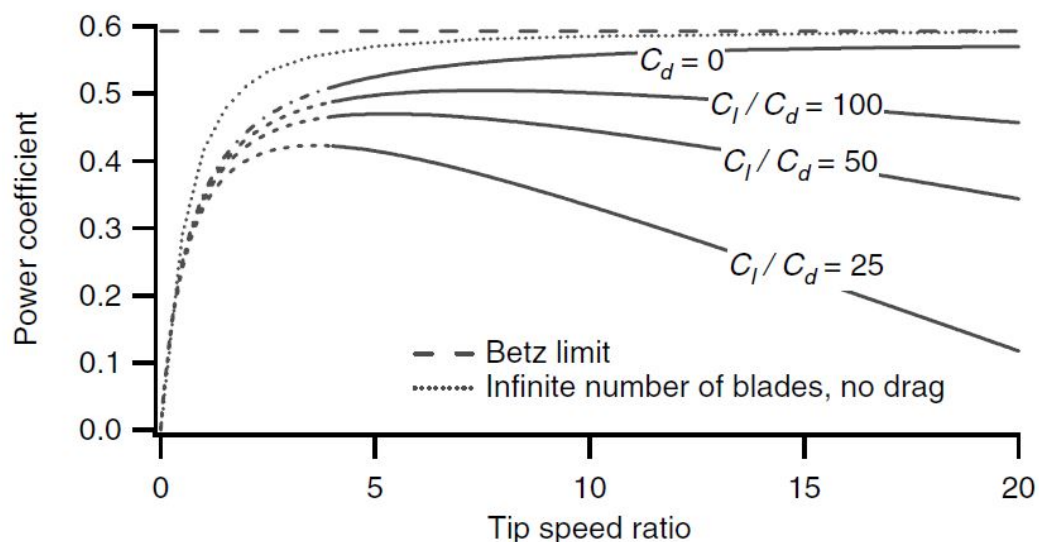**Figure 3.7:** Maximum achievable power coefficients as a function of number of blades, no drag

Figure 3.8: Maximum achievable power coefficients of a three-bladed optimum rotor as a function of the lift to drag ratio, C_l/C_d

The one and two bladed rotors need to rotate at a higher rotational speed to obtain the same 'solidity' and thereby power production as for the three bladed rotor. This will increase the acoustic noise emission, but for offshore application it may not be a problem. Still, the one bladed rotor will need a large counterweight (to balance the static rotor weight). From that point of view the two bladed rotor is a better option. For stability issues the two bladed rotor may be exposed to large cyclic loads originating from the fluctuating rotational inertia about the yaw axis. And with the higher rotational speed for both the one and two bladed rotors, blade edge erosion could occur, which would tremendously increase the offshore maintenance costs.

3.c.iv   Blade Shape Optimization with Wake Rotation

Similarly to Section 2.c (Horizontal Axis Wind Turbine with Wake Rotation), here the optimized shape of a blade including wake rotation can be calculated neglecting drag ($C_D = 0$) and tip losses ($F = 1$). Following the procedure of taking partial derivatives of the power coefficient expression introduced by de Vries (Equation 3.29) and equalizing it to zero to maximize it:

$$\frac{\partial}{\partial \varphi}[sin^2\varphi(cos\varphi - \lambda_r sin\varphi)(sin\varphi + \lambda_r cos\varphi)] = 0 \tag{3.32}$$

$$\lambda_r = sin\varphi \frac{(2cos\varphi - 1)}{(1 - cos\varphi)(2cos\varphi + 1)} \tag{3.33}$$

With this data the following relations are made:

$$\varphi = \frac{2}{3}tan^{-1}(1/\lambda_r) \tag{3.34}$$

$$c = \frac{8\pi r}{BC_l}(1 - cos\varphi) \tag{3.35}$$

Comparing Equations 3.34 and 3.35 to the ones obtained without wake rotation (Equations 3.15 and 3.17) one can see that the effects of wake are, often, minimum. However, the effects

could be significant for some cases.

Local solidity was introduced before, and now the concept of solidity as the ratio ratio of the planform area of the blades to the swept area is presented in Equations 3.36 and 3.37:

$$\sigma = \frac{1}{\pi R^2} \int_{r_h}^{R} c\, dr \tag{3.36}$$

$$\sigma \cong \frac{B}{N\pi} \left(\sum_{i=1}^{N} c_i / R \right) \tag{3.37}$$

Note that Equation 3.37 models the solidity for N blade sections for obtaining the optimum. Here the blade twist is directly related to the angle of the relative wind due to the fact that the angle of attack is assumed to be constant, and therefore a change in the blade twist would make the same changes in the angle of the relative wind.

3.d Wind Turbine Design Procedure

Manwell [5] presents a usefull simplified HAWT rotor calculation procedure, however, a series of more detailed steps will be presented here so that the procedure and use of equations presented along the previous sections and analysis is clear. In the first approach, only wake rotation will be taken into account, in order to obtain an initial blade shape. After that, iterative calculations will take into account drag, tip losses, and ease of manufacture to get the final blade shape.

1. First step will be choosing an appropriate power (P) that the wind turbine is going to generate. Then an indicative wind velocity (U), a probable C_P and general efficiencies (η) considering mechanical losses, losses of the gearbox, pump losses, etc. will be added to Equation 3.38, which will give an estimation of the radius (R):

$$P = \frac{1}{2} C_P \eta \rho \pi R^2 U^3 \tag{3.38}$$

2. Next, a tip speed ratio (λ) will be chosen according to the application of the turbine, for instance, for a water-pumping windmill, for which greater torque is needed, use $1 < \lambda < 3$.

For electrical power generation, use $4 < \lambda < 10$. The higher speed machines use less material in the blades and have smaller gearboxes, but require more sophisticated airfoils.

3. After that, the number of blades can be selected from the suggested values presented in Table 2.

λ	B
1	8-24
2	6-12
3	3-6
4	3-4
>4	2-3

Table 2: Suggested blade number, B, for different tip speed ratios, λ

4. Airfoil selection bearing in mind the purpose of the blades. The curves for the aerodynamic properties must be studied and the design conditions established ($C_{l,design}$ and α_{design} for $C_{d,design}/C_{l,design}$ is the minimum possible.

5. In order to simplify calculus, the blade needs to be divided in N elements (≈ 20) and using the theory shown in previous sections a first approach of the blade shape can be made for each element i:

$$\lambda_{r,i} = \lambda(r_i/R) \tag{3.39}$$

$$\varphi_i = \frac{2}{3}tan^{-1}(1/\lambda_{r,i}) \tag{3.40}$$

$$c_i = \frac{8\pi r}{BC_{l,design,i}}(1 - cos\varphi) \tag{3.41}$$

$$\theta_{T,i} = \theta_{p,i} - \theta_{p,0} \tag{3.42}$$

$$\varphi_i = \theta_{p,i} + \alpha_{design,i} \tag{3.43}$$

6. Regarding ease of manufacture, after calculating the optimum blade shape as a guide, one can use linear variations of chord, thickness and twist that get as close as possible to the optimum design but saving a lot of effort in the manufacturing process.

$$c_i = a_1 r_i + b_1 \tag{3.44}$$

$$\theta_{T,i} = a_2(R - r_i) \tag{3.45}$$

7. Now one of the two methods described previously must be applied to determine flow conditions and forces at each blade section.

- *Method 1 - Solving C_l and α*
  The angle of attack and lift coefficient can be calculated using the empirical airfoil curves and the following equations:

$$C_{l,i} = 4F_i sin\varphi_i \frac{(cos\varphi_i - \lambda_{r,i} sin\varphi_i)}{\sigma_i'(sin\varphi_i + \lambda_{r,i} cos\varphi_i)} \tag{3.46}$$

$$\sigma_i' = \frac{Bc_i}{2\pi r_i} \tag{3.47}$$

$$\varphi_i = \alpha_i + \theta_{T,i} + \theta_{P,0} \tag{3.48}$$

$$F_i = \frac{2}{\pi}cos^{-1}\left\{exp\left[-\left(\frac{(B/2)[1-(r_i/R)]}{(r_i/R)sin\varphi_i}\right)\right]\right\} \qquad (3.49)$$

For the iterative process an initial estimation of F_i is needed using $\varphi_{i,1} = \frac{2}{3}tan^{-1}(1/\lambda_{r,i})$ for the first iteration and then $\varphi_{i,j+1} = \theta_{P,i} + \alpha_{i,j}$, where j is the number of iterations (usually only a few are needed). Finally the axial induction factor is calculated:

$$a_i = \frac{1}{[1+\frac{4sin^2\varphi_i}{\sigma_i' C_{l,i} cos\varphi_i}]} \qquad (3.50)$$

If a_i is greater than 0.4, Method 2 must be used.

As stated in the solution method, this method can also be solved graphically plotting the empirical C_l vs. α curves for the chosen airfoil and Equation 3.46 (see Figure 3.9).
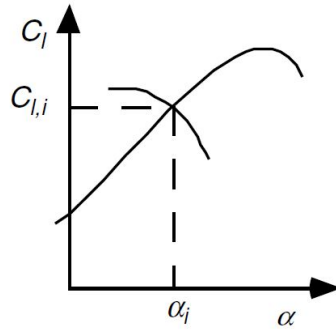
Figure 3.9: Graphical solution for angle of attack, a; C_l , two-dimensional lift coefficient; $C_{l,i}$ and a_i , C_l and a, respectively, for blade section, i

- *Method 2 - Iterating a and a′*
  It was indicated that this method was especially useful for highly loaded rotor conditions $(a_i > 0.4)$, so following the steps presented in the solution method presentation:

  First step is guessing values of a and a'. Use $\varphi_{i,1} = \frac{2}{3}tan^{-1}(1/\lambda_{r,i})$ for the first iteration (as in the previous method), then:

$$a_{i,1} = \frac{1}{[1 + \frac{4sin^2\varphi_{i,1}}{\sigma'_{i,design}C_{l,design}cos\varphi_{i,1}}]}$$ (3.51)

$$a'_{i,1} = \frac{1 - 3a_{i,1}}{4a_{i,1} - 1}$$ (3.52)

After the initial iterations, the angle of the relative wind and the tip loss factor can be calculated:

$$tan\varphi_{i,j} = \frac{U(1 - a_{i,j})}{\Omega r(1 + a'_{i,j})} = \frac{1 - a_{i,j}}{(1 + a'_{i,j})\lambda_{r,i}}$$ (3.53)

$$F_{i,j} = \frac{2}{\pi}cos^{-1}\left\{exp\left[-\left(\frac{(B/2)[1 - (r_i/R)]}{(r_i/R)sin\varphi_{i,j}}\right)\right]\right\}$$ (3.54)

Now $C_{l,i,j}$ and $C_{d,i,j}$ and the local thrust coefficient ($C_{Tr,i,j}$) can be determined using:

$$\alpha_{i,j} = \varphi_{i,j} - \theta_{p,i}$$ (3.55)

$$C_{Tr,i,j} = \frac{\sigma'_i(1 - a_{i,j})^2(C_{l,i,j}cos\varphi_{i,j} + C_{d,i,j}sin\varphi_{i,j})}{sin^2\varphi_{i,j}}$$ (3.56)

Now if $C_{Tr,i,j} < 0.96$, only a must be updated:

$$a_{i,j+1} = \frac{1}{[1 + \frac{4F_{i,j}sin^2\varphi_{i,j}}{\sigma'_iC_{l,i,j}cos\varphi_{i,j}}]}$$ (3.57)

43

on the other hand, if $C_{T_r,i,j} > 0.96$, both a and a' must be updated:

$$a_{i,j} = \frac{1}{F_{i,j}} \left[0.143 + \sqrt{0.0203 - 0.6427(0.889 - C_{T_r,i,j})} \right] \qquad (3.58)$$

$$a'_{i,j+1} = \frac{1}{\left[\frac{4F_{i,j}cos\varphi_{i,j}}{\sigma'_i C_{l,i,j}} \right] - 1} \qquad (3.59)$$

The iterations must be repeated until the induction factors have little error with respect the previous guesses and they are within an acceptable range of values, otherwise another design values should be taken and the process must be repeated.

8. Once all the elements of the blade have been calculated, the power coefficient can be determined using:

$$C_P = \frac{8}{\lambda^2} \sum_{i=1}^{N} F_i sin^2\varphi_i(cos\varphi_i - \lambda_{r,i}sin\varphi_i)(sin\varphi_i + \lambda_{r,i}cos\varphi_i) \left[1 - \frac{C_d}{C_l}cot\varphi_i \right] \lambda_{r,i}^2 \quad (3.60)$$

In case the power coefficient is not sufficiently high or the desired one, the design conditions can be changed and recalculated.

3.e $C_P - \lambda$ Curves and Controllability

Once the blade has been designed for optimum operation at a specific design tip speed ratio, the performance of the rotor over all expected tip speed ratios needs to be determined, and the results are presented in a $C_P - \lambda$ curve. They provide immediate information on the maximum rotor power coefficient and optimum tip speed ratio.

All wind turbines are designed for a maximum wind speed, called the survival speed, above which they will be damaged. The survival speed of commercial wind turbines is in the range of 40 m/s (144 km/h, 89 MPH) to 72 m/s (259 km/h, 161 MPH). The most common survival speed is 60 m/s (216 km/h, 134 MPH). And due to the high power requirements of wind turbines, it is necessary to ensure that the automatic control of the rotor is correctly applied and can be controlled in every situation. Therefore, in order to make sure that the automatic

control does not have to apply an unacceptable brake torque at high wind velocities, the turbine must be effectively stall-regulated.

In this aspect, as indicated in the publication of A. Torregrosa et al.[6], the left slope of the blade non dimensional power curve is found to be a key design parameter, in order to obtain a design able to produce power in a wide range of wind velocities avoiding the risk of uncontrollable conditions.

As it can be seen in Equation 2.27, the power scales with the relation $P \alpha C_p U^3$, and since the stall-regulated condition implies $\frac{dP}{dU} < 0$ for the maximum expected wind velocity, the following expression can be determined:

$$\frac{dC_P}{d\lambda} > \frac{3C_P}{\lambda} \qquad (3.61)$$

Equation 3.61 means that the higher the left slope in the $C_P - \lambda$ curve is, the better controllability the rotor will have, since a small reduction in the velocity (and therefore λ) implies a fast decrease in power generated, thus preventing the wind turbine from excessive loads.

3.f Non-ideal Steady State, Turbine Wakes and Unsteady Aerodynamic Effects

All the previous sections predicted the wind turbine performance as a function of steady state aerodynamics, with most ideal assumptions, without taking into account most of the dynamics effects. An introduction of these effects is presented in this section [5], including non-ideal steady state effects, the influence of turbine wakes, and unsteady aerodynamics.

3.f.i Non-ideal Steady State Aerodynamic Issues

Here effects such as surface roughness, stall and blade rotation are included. For instance the deterioration and dirt of the surface can decrease up to a 40% [5], and the only solution is investing on maintenance and better blade materials. Regarding stall conditions, fluctuating loads arise, yielding rapidly fluctuating flow conditions and rapidly fluctuating loads on the wind turbine. Then, experimental testing on the blades is done without rotation, but when the blades are on an horizontal wind turbine, they may produce more power than expected and delayed stall conditions due to rotation, which might shorten the life of the blade since the conditions tested were 'smoother' than the real ones.

3.f.ii   Unsteady Aerodynamic Effects

Aerodynamic forces are not steady due to several phenomena such as turbulent eddies, blade vibrations, material fatigue... Tower shadow, dynamic stall and inflow and rotational sampling are other effects that change the performance unexpectedly and occur at the rotational frequency of the rotor or at multiples of that frequency.

The effect of wind distorsion behind a windmill is known as *tower shadow*, which affects each blade once per revolution, causing a deficit of power and vibrations along the structure. More about the effect of tower shadow in downwind wind turbines can be read in the thesis of Marit Reiso [17].

Dynamic stall is defined as the sudden changes in aerodynamics that cause stall conditions variations, such as delay. Rapid changes in wind speed (for example, when the blades pass through the tower shadow) cause a sudden detachment and then reattachment of air flow along the airfoil. Such effects at the blade surface cannot be predicted with steady state aerodynamics, but may affect turbine operation, not only when the blades encounter tower shadow, but also during operation in turbulent wind conditions. Dynamic stall effects occur on time scales of the order of the time for the relative wind at the blade to traverse the blade chord, approximately $c/\Omega r$. For large wind turbines, this might be on the order of 0.2 seconds at the blade root to 0.01 seconds at the blade tip according to Snel and Schepers [14].

Next, the *dynamic inflow* can be described as the response of the larger flow field to turbulence and changes in rotor operation. Steady state aerodynamics suggest that increased wind speed and, thus, increased power production should result in an instantaneous increase in the axial induction factor and changes in the flow field upstream and downstream of the rotor. During rapid changes in the flow and rapid changes in rotor operation, the larger field cannot respond quickly enough to instantly establish steady state conditions. Thus, the aerodynamic conditions at the rotor are not necessarily the expected conditions, but an ever-changing approximation as the flow field changes. The time scale of dynamic flow effects is on the order of D/U, the ratio of the rotor diameter to the mean ambient flow velocity. This might be as much as ten seconds again according to Snel and Schepers[14]. Phenomena occurring slower than this can be considered using a steady state analysis.

Finally, *rotational sampling* increases fluctuating loads on the wind turbine due to unsteady aerodynamic effects, since the wind is relatively seen by the rotor and this is constantly changing, which could bring wind speed changes on a time scale of about five seconds.

3.f.iii   Turbine Wakes

This effect was described along several sections such as Section 2.c for the whole wind turbine, and Section 3.c for the specific blade effect. However, the actual effect is much more complicated. This wake affects the performance of the whole group of wind turbines (downwind wind turbines), and may result in a 'skewed wake,' which causes increased fluctuating loads which are not predicted by BEM theory.

First, one must differentiate between near and far wake, each of them characterized by the spatial distribution and the intensity of the turbulence in the flow field. Then, according to Voutsinas et al.[15], a blade generates vortices not only on the tips (which are the ones mentioned in Section 3.c.ii and the most important ones), but on the trailing edge and on the hub as well, which convert downstream. The periodic nature of the vortex flow is lost in the near wake (Ebert and Wood[16]), therefore creating an evenly distributed turbulence and velocity profiles in the far wake. The free stream wind recharges the flow and mixing and diffusion continue in the far wake until the turbulence and velocity difference with respect to the free stream flow have dissipated. The vortex sheet from the tip vortices results in an annular area in the far wake of higher relative turbulence surrounding the less turbulent core of the wake.

The effects of these wakes are material fatigue, which is not negligible on wind farms where the wake may affect several wind turbines downwind and increased loads, which reduce the energy transformed by the blades.

4 Fluid Dynamic Modelling

This section will include the description of the analysis of a wind turbine on Simcenter Star-CCM+, a commercial Computational Fluid Dynamics (CFD) based simulation software, in which more effects can be modelled and in most cases replace expensive experiments which require high end test facilities. Most information regarding the program setup and configuration has been recollected from the STAR-CCM+ Product Overview[21].

4.a Turbulence modelling

There are a few different methods that can be used to properly model the flow around a wind turbine. The most widely used of these is the Reynolds averaged Navier-Stokes turbulence model (RANS). Fluid mechanics governing equations are the one used to characterize the flow, and in this case a simplification is made by taking various assumptions in order to be able to solve them. RANS is a turbulent flow model, which solves the Navier-Stokes equations by using the mean flow. Therefore, the sets of equations that are used are time-averaged. This is a very common method used for computation fluid modeling and it is frequently applied to wind turbine models because it yields fairly accurate results within a relatively short computation time.

$$\rho \left(\frac{\partial u}{\partial t} + u \frac{\partial u}{\partial x} + v \frac{\partial u}{\partial y} + w \frac{\partial u}{\partial z} \right) = -\frac{\partial p}{\partial x} + \mu \left(\frac{\partial^2 u}{\partial x^2} + \frac{\partial^2 u}{\partial y^2} + \frac{\partial^2 u}{\partial z^2} \right) + \rho g_x$$

$$\rho \left(\frac{\partial v}{\partial t} + u \frac{\partial v}{\partial x} + v \frac{\partial v}{\partial y} + w \frac{\partial v}{\partial z} \right) = -\frac{\partial p}{\partial y} + \mu \left(\frac{\partial^2 v}{\partial x^2} + \frac{\partial^2 v}{\partial y^2} + \frac{\partial^2 v}{\partial z^2} \right) + \rho g_y \quad \text{(Navier-Stokes equation)}$$

$$\rho \left(\frac{\partial w}{\partial t} + u \frac{\partial w}{\partial x} + v \frac{\partial w}{\partial y} + w \frac{\partial w}{\partial z} \right) = -\frac{\partial p}{\partial z} + \mu \left(\frac{\partial^2 w}{\partial x^2} + \frac{\partial^2 w}{\partial y^2} + \frac{\partial^2 w}{\partial z^2} \right) + \rho g_z$$

$$\frac{\partial \rho}{\partial t} + \left(\frac{\partial \rho u}{\partial x} + \frac{\partial \rho v}{\partial y} + \frac{\partial \rho w}{\partial z} \right) = 0 \quad \text{(Continuity equation)}$$

where the term at the left part of the Navier-Stokes Equation represents the convective forces, the derivative of pressure is the pressure gradient, the μ term is the viscous effects one (diffusion term) and finally the last term represents the body forces acting. For Navier-Stokes equation and Continuity equation, u represents the velocity in the x direction, v in the y direction and w is the velocity in the z axis. The Continuity equation states that the rate at which mass enters a system is equal to the rate at which mass leaves the system plus the accumulation of mass within the system, which is necessary for the calculations.

When choosing between the different variants of a model, one must take into account the behavior of the fluid near the wall, and its relationship with the size of the mesh in it, and

then is when the wall y^+ plays a major role:

$$y^+ = \frac{yu^*}{\nu} \tag{4.1}$$

where y is distance from the wall to the centroid of the first cell, u^* is friction velocity and ν is the kinematic viscosity as referenced above. For the calculation of the turbulent boundary layer, one can use what is known as the Law of the wall, which is a logarithmic law that relates the velocity in the boundary layer to the value of y^+. There are two types of Law of the wall:

- *Standard wall laws*, in which velocities transition between laminar and turbulent flow occur with a discontinuity.

- *Blended wall laws*, in which this transition is gradual, and this region is known as *buffer region*.

One cannot choose the law explicitly, since they are bounded to each type of model. However, mesh size must be taken into account in order to fit y^+ values: the finer the mesh and the lower the flow velocity, the lower will be the values of y^+. In this case three types of wall treatment can be chosen:

- *High-y^+ wall treatment*: assumes that the cell closest to the wall is within the logarithmic region and therefore makes use of the law of the wall.

- *Low-y^+ wall treatment*: It is only valid for low Reynolds numbers. Requires a mesh sufficiently fine, and the higher the Reynolds number, the finer the mesh must be. Therefore, it is computationally expensive. This treatment resolves the viscous boundary layer without need to make use of the law of the wall.

- *All-y^+ wall treatment*: this treatment is a hybrid of the previous ones. It makes use of the former one when the cell is within the logarithmic region, and the latter if the cell is within the viscous region (very fine mesh) and is also valid if the cell is in the laminar-turbulent transition region (*buffer region*).

There are several turbulence models that can be applied depending on the system that has to be modelled. The most common ones are $k - \varepsilon$, $k - \omega$ and *Spalart-Allmaras* turbulence models. These three models are all eddy viscosity models, which use the Reynolds-averaged Navier-Stokes and turbulent viscosity to model the Reynolds stress tensor as a function of the average flow. The $k - \varepsilon$ and $k - \omega$ models are two-equation models, while *Spalart-Allmaras* uses only one equation. Now a description on each model will be made based on David C. Wilcox [18].

4.a.i $k - \varepsilon$ model

The $k - \varepsilon$ model is characterized by $\nu_T = \nu_T(k, \varepsilon)$ (kinematic viscosity is dependent of the variables k and ε), where k is the turbulent kinetic energy and ε the turbulent kinetic energy dissipation rate. So as to determine the expression of ν_T and of k and ε, it is necessary to use results of simpler flows whose theoretical or experimental solution are known. The software has up to 8 different $k - \varepsilon$ models.

4.a.ii $k - \omega$ model

As the previous model, the $k - \omega$ model makes use of two variables: k is the turbulent kinetic energy, as before, and ω is the specific dissipation rate, that is, the dissipation per unit of turbulent kinetic energy ($\omega \sim \frac{\varepsilon}{k}$). The software has two different $k - \omega$ models.

For this project, this model has been used, more specifically the SST (Menter) K-Omega. The Shear Stress Transport K-Omega model takes advantage of accurate formulation of the K-Omega model in the near-wall region with the free-stream independence of the K-Epsilon model in the far field. It does so multiplying a final additional term, obtained from deriving the K-Epsilon model, by a blending function. Close to wall the damped cross-diffusion derivative term is zero (leading to the standard ω equation), whereas remote from wall the blending function is unity (corresponding to the standard ε equation).

4.a.iii   Spalart-Allmaras model

This model solves the equations by introducing a single variable: turbulent viscosity kinematics. It was originally created for the aerospace industry and for low Reynolds number, as well as for values $y^+ \sim 1$, although currently there are less restrictive models. Star-CCM+ presents up to three possible variants of this model.

4.a.iv   Reynolds Stress Transport model

Another form of RANS turbulence model available is the Reynolds Stress Transport model. Unlike the other turbulence models, this is not an eddy viscosity model, since it solves for all components of the Reynolds stress tensor, rather than focusing on viscosity like the eddy viscosity models. It is best suited for situations when the flow is very anisotropic, which means that it varies greatly depending on direction.

4.a.v   Detached Eddy Simulation

Detached eddy simulation (DES) is often used for situations when the unsteadiness in the flow is "imposed or inherent," such as when the boundary conditions are changing significantly with time or there is massively separated flow.

4.a.vi   Large Eddy Simulation

Another common method that arose more recently than RANS is Large-Eddy Simulation, or LES. This method differs from RANS in that it removes the smaller aspects of the flow in order to model the large turbulent eddies, thus capturing the larger structures of the flow more accurately. Therefore, rather than averaging the flow, it filters out the small-scale information in the flow, which simplifies the model so that the large aspects of the flow can be modeled directly. While it has been acknowledged that this method typically yields more accurate results (LES does a much better job at capturing the turbulent mixing of the airflow) than the RANS turbulence model, it requires far more computational time, and is not always a viable option.

4.b   Simulation Setup

4.b.i   General guides

The main goal of this project is to calculate power values for wind turbines, being the flow a secondary aspect of the simulations that will be analyzed. Therefore the complexity of a LES model would have been superfluous , since a RANS model and a LES have the same capability to determine power generated.

For the geometry, it is the NREL Phase VI blade, depicted in Figure 4.1, used in several documents like the paper published by Antonio Torregrosa et al[6] . The blade radius (5.029 m) was set as a parameter to build the fluid region and set another variables with respect to this measure.
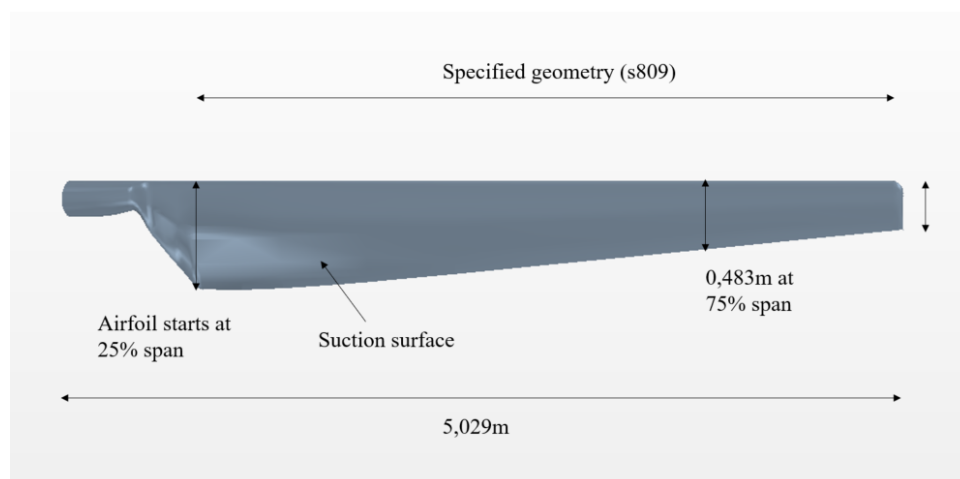

Figure 4.1: Shape model of the NREL Phase VI wind turbine blade

Around this geometry, a part with the shape of a truncated cone was created in order to simulate the flow region in Star-CCM+, obtaining the fluid zone by substracting the blade shape from that cone. Moreover, in order to get 2-bladed, 3-bladed and 4-bladed turbines, this

cone was cut in half (Figure 4.2), withing 120° (Figure 4.3) and 90° (Figure 4.4) respectively, as will be seen in the following section (Section 4.b.ii). Then the different regions and domain were set, leading to the physics and mesh conditions. As previously stated, the model K-Omega SST (Menter) was used, and standard atmosphere conditions. Regarding motions, it must be said that a moving reference frame was set in order to solve the case, where the geometry of the blade rotates with that reference frame, so that the fluid is steady from that point of view. This reference frame rotates with the relation of the tip speed ratio parameter, λ, and a constant wind velocity of 10 m/s (Equation 2.24). Finally one can configure different meshes and compute some solutions in order to check with the references and determine which is the best one to carry the rest of the calculus, following the workflow shown in Figure 1.3.

4.b.ii Geometry and region definition

For the NREL Phase VI blade, 3 different setups were set, obtaining three types of turbines: a 2-bladed, 3-bladed and 4-bladed, whose blade geometry is the same, while the region definition varies according to Figures 4.2, 4.3 and 4.4:

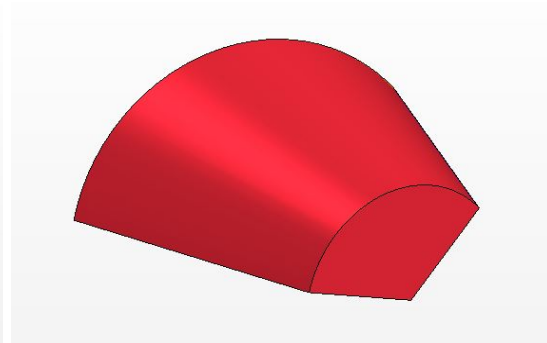**Figure 4.2:** 2-bladed computational domain

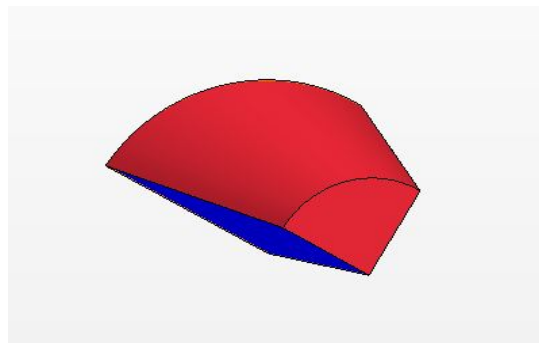**Figure 4.3:** 3-bladed computational domain

Figure 4.4: 4-bladed computational domain

For all the geometries, the front wall (radius 3 times the blade radius and 2 radius ahead) was set as a velocity inlet, the back (radius 6 times the blade radius and 4 radius behind) was defined as a pressure outlet and, for the outer cylindrical region, the far field, it was set as a velocity inlet in the same way as the front wall. This boundary condition is important because

if the wall was set as no-slip wall, the velocity of the flow at the wall would be zero, meaning the flow would not only be affected by the rotating turbine, it would also be heavily influenced by the wall. Moreover, all the setups have a periodic condition set in the lower parts, being able to define the number of blades thanks to the angle formed between them: 180° for the 2-bladed, 120° for the 3-bladed turbine and 90° for the 4-bladed one. This periodic condition was configured through an interface created with a symmetry plane in the region section between the two blue planes (the ones that change its angle between setups) of Figure 4.6. In Figure 4.5 the geometry distances is depicted as well.
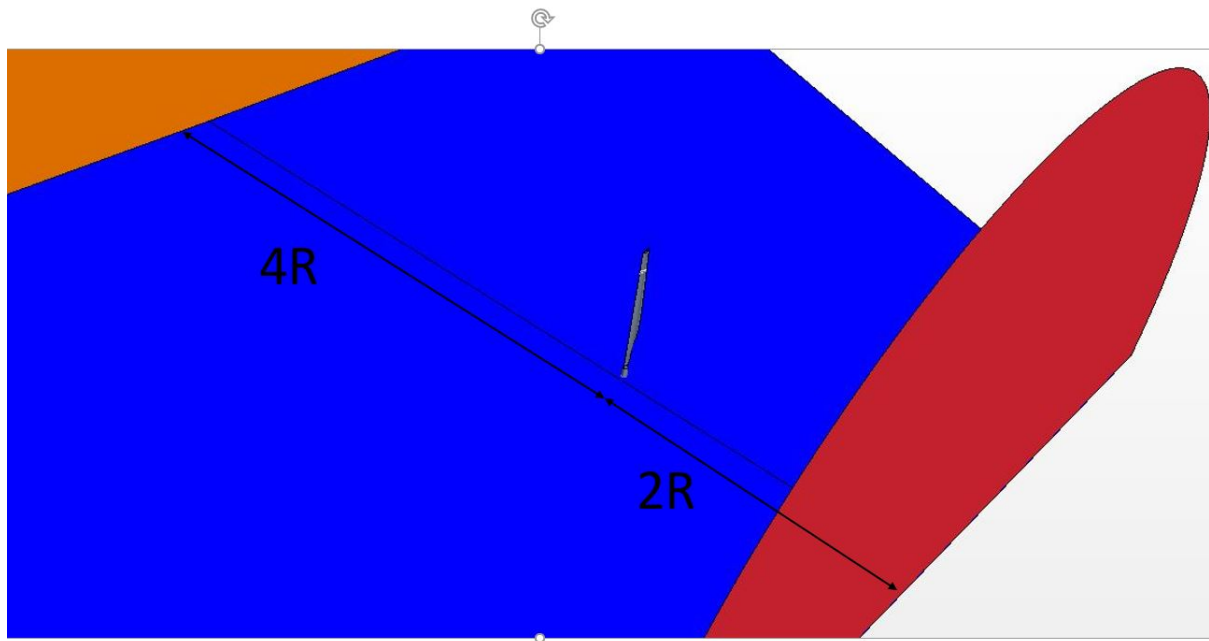

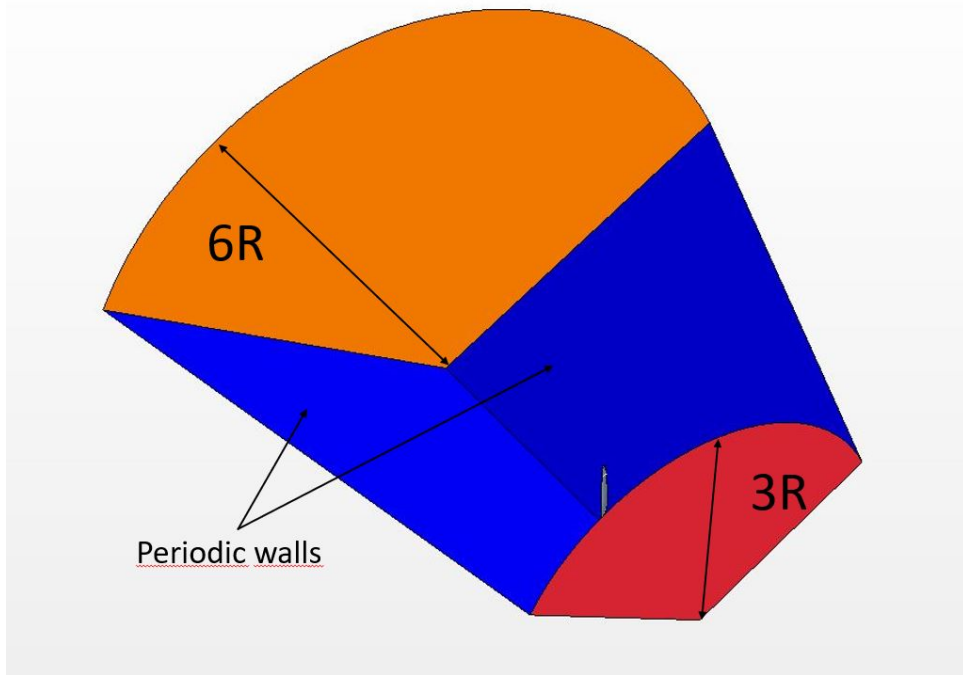**Figure 4.5:** Distance and geometry setups in the 2 bladed configuration

Figure 4.6: Distance and geometry setups in the 3 bladed configuration

4.b.iii Continua Physics and Mesh

As previously mentioned, the physics make use of the SST $k - \omega$ model with an all y^+ wall treatment. This study was conducted with steady, turbulent flow, which was defined as incompressible because there are no changes in density as the air travels through the turbine, since air stays at a very low velocity compared to the velocity of sound. Moreover, the reference pressure was set at 101325 Pa, and air conditions set to the ones found in literature: a density of 1.18415 kg/m^3 and a dynamic viscosity of $1.7894 \cdot 10^{-5}$ Pa·s. An implicit coupled flow solver was selected, so the conservation equations for continuity, momentum, energy, and species are solved in a coupled manner, that is, they are solved simultaneously as a vector of equations. The velocity field is obtained from the momentum equations. From the continuity equation, the pressure is calculated and the density is evaluated from the equation of state. The Courant Number (CFL) property of the Coupled Implicit and Coupled Explicit solvers controls the size of the local time-steps that are used in the time-marching procedure these two solvers employ. The Courant number plays the same role as under-relaxation parameters in the segregated solver.

Regarding meshing conditions, a base size of half the radius of the blade was set, an essential point, due to the the fact that all the other parameters in the meshing part are calculated with respect to that value.

It should be remarked that the most complicated part of this study was determining the best mesh to use. There have been (among many other failed attempts) two types of meshes, with the only difference of the boundary layer thickness between them. Both were done with

a polyhedral mesher, surface remesher and of course a prism layer mesher for solving the boundary layer. Both had 15 prism layers and a stretching factor of 1.2, with thicknesses of 0.5 cm and 0.32 cm, yielding better results the latter, as will be shown in Section 4.c. for both the wall y^+ stayed under 1 for most of its cells, and since the all y^+ treatment was applied, we can count for the boundary layer to have been correctly solved and transitioned to the free stream flow.
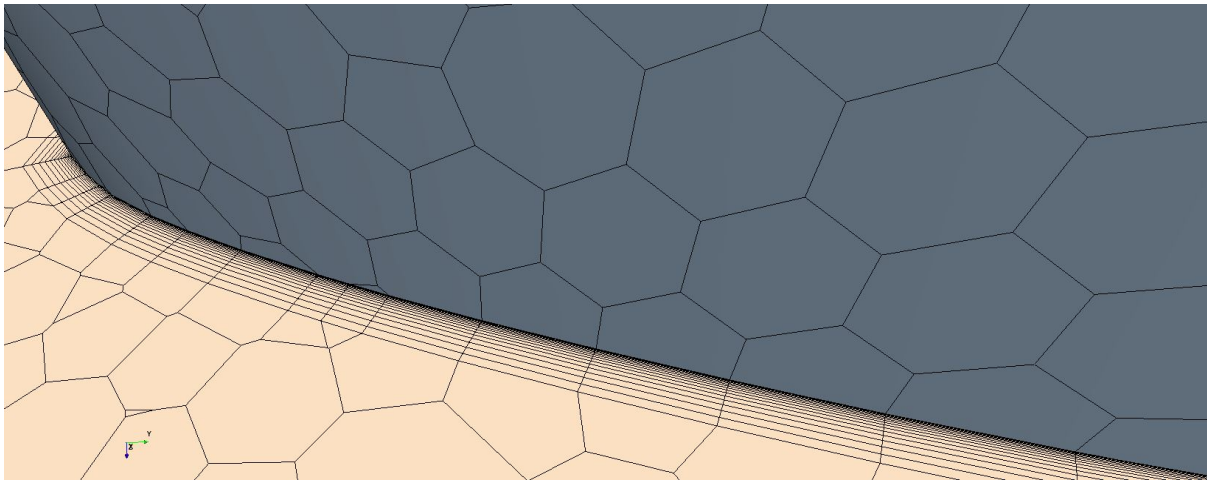

Figure 4.7: Boundary layer meshing

Moreover, two volumetric controls were created to refine the mesh and make it smaller in certain parts closer to the blade, as Figures 4.8 and 4.9, and the resulting mesh can be seen in Figure 4.10:
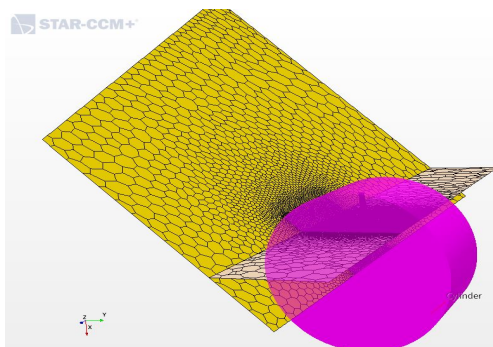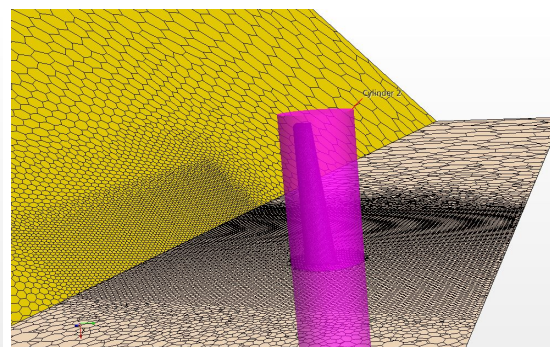

Figure 4.8: Volumetric control 1

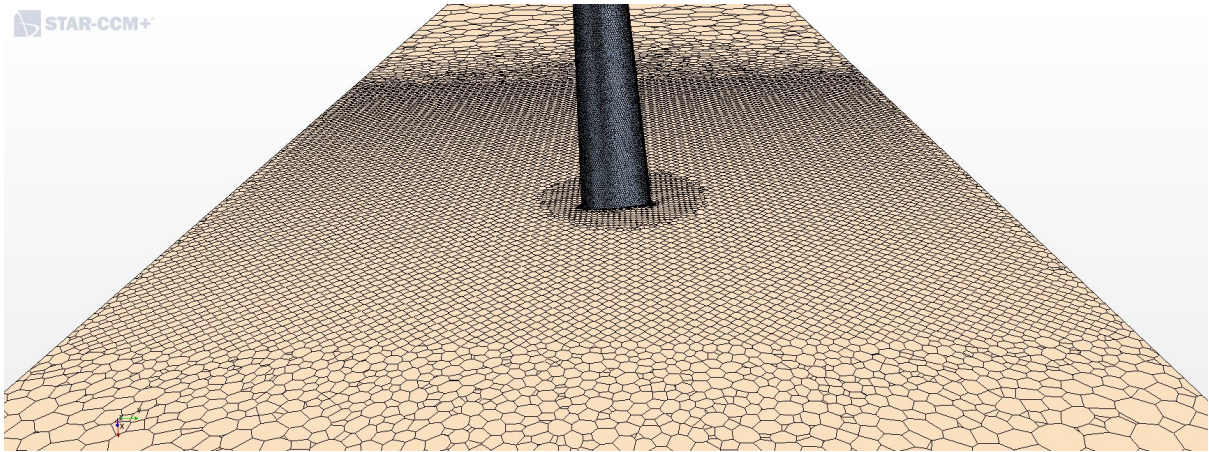**Figure 4.9:** Volumetric control 2

Figure 4.10: Meshing regions depending on control volumes

It can be seen how by doing this, the mesh will need less cells than meshing all with the same size, since one can focus on the parts that need more computational effort, while saving computational costs in the outter regions where the flow will not affect in the same way. More details on the mesh can be seen in the following pictures (Figures 4.11 and 4.12).
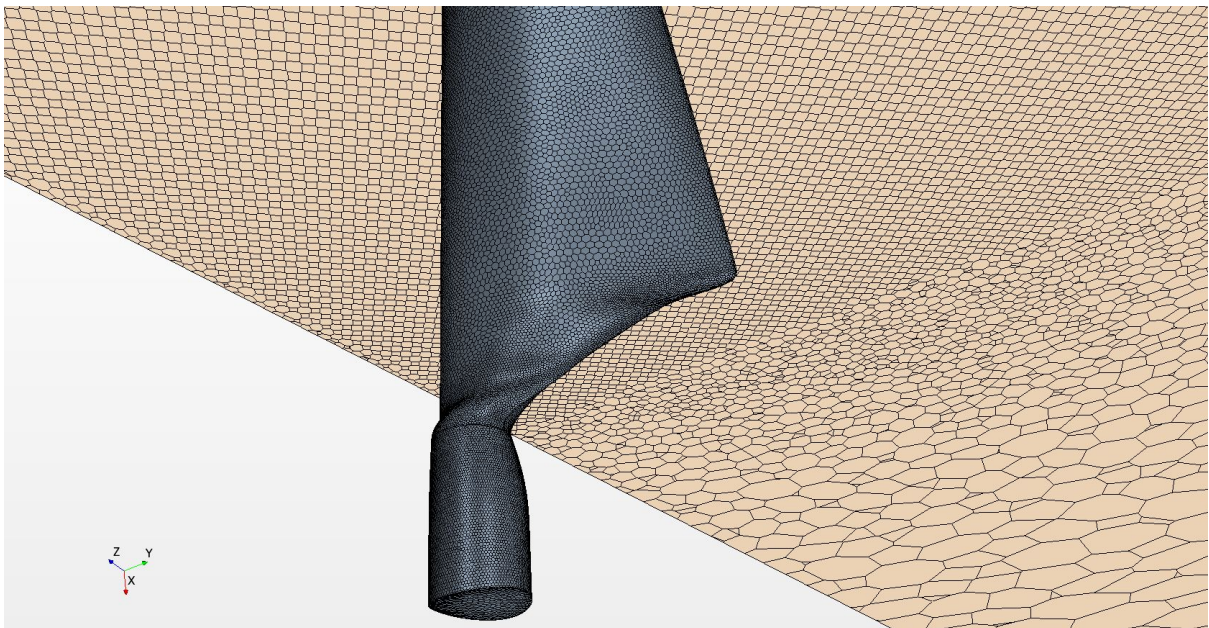

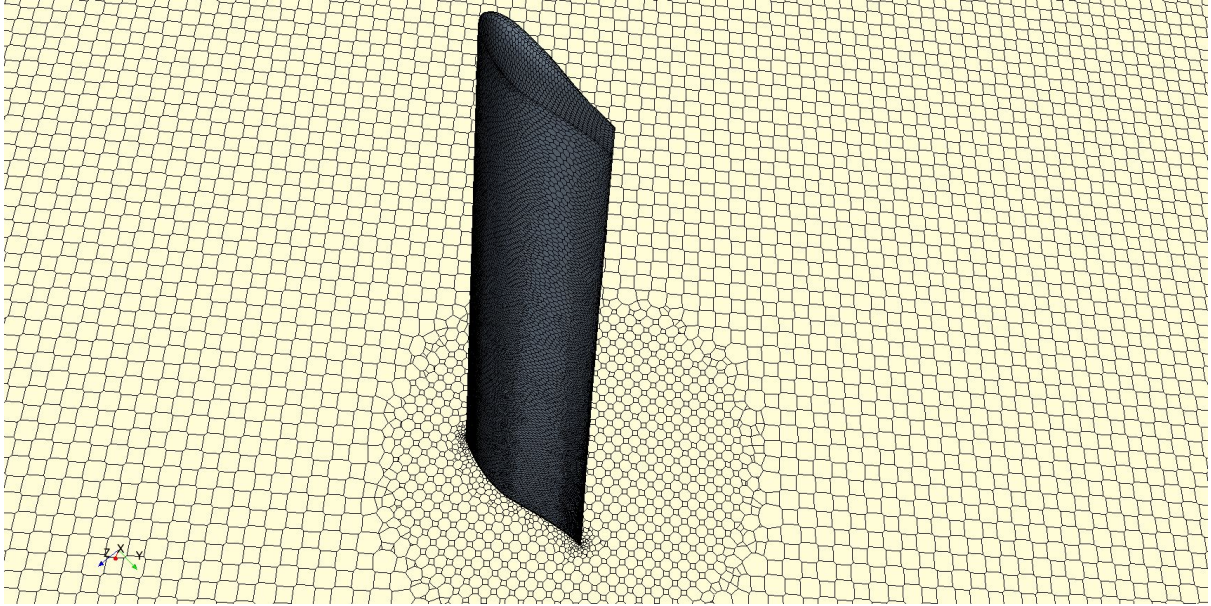**Figure 4.11:** Meshing details from hub perspective

Figure 4.12: Meshing details from tip perspective

4.b.iv   Initial Conditions and Motion

The three different geometries have been studied for 11 different λ (which relates the inlet velocity (10 m/s) with the rotational rate Ω with Equation 2.24). The tip speed ratios begin at 0, which obviously yields null angular velocity and results, until $\lambda = 11$, resulting in $\Omega \approx 200$ rpm (which would correspond to velocities in the tip of up to $v_{tip} = R \cdot \Omega \approx 110$ m/s), a highly excessive rotation rate, but in this way all type of conditions will be studied withing a wide range. Table 3 outlines the velocities and rates studied for the three models of wind turbines.

λ	Ω (rad/s)	Ω (rpm)
1	1.91	18.26
2	3.82	36.52
3	5.74	54.79
4	7.65	73.05
5	9.56	91.31
6	11.47	109.57
7	13.39	127.84
8	15.30	146.10
9	17.21	164.36
10	19.12	182.62
11	21.04	200.88

Table 3: Conversion of velocities for the different conditions studied

For the velocity inlet, as just stated, a velocity of 10.0 m/s along the z-axis (negative direction) was set, a medium-fast wind velocity at low altitudes.The initial free stream velocity was also set to -10.0 m/s in the direction of the z-axis.

And as previously mentioned, the reference pressure was set at 101325 Pa, and air conditions set to the ones found in literature: a density of 1.18415 kg/m^3 and a dynamic viscosity of $1.7894 \cdot 10^{-5}$ Pa·s, with a null initial pressure.

4.c   Analysis of Results

In this chapter results will be compared for different cases. For reasons of time, resources and the great variety of parameters that influence the problem, only the number of blades has been changed from the turbines. The rest of the geometry and the atmosphere has remained invariable.

The first calculation after the meshing was the power and force generated by each wind turbine, in order to validate it with data from the NREL Phase VI and other bibliographic resources.

The long way of determining the power generated by the turbine is to integrate the pressure over the blade to find the force along it, then one can use the force and the radius of the blades to find torque. Finally, the dot product of torque and angular velocity is taken to calculate power generated (Equation 2.27.) On Star-CCM+ the torque of the turbine can be determined directly by creating a moment report for the turbine and ensuring that the axis origin is located at the origin of the turbine. The power can then be calculated directly by using the value for torque found by the report. After several iterations, the calculations of the power generated by each turbine, in this case expressed as the power coefficient (Equation 2.12) and the normal force, represented by the thrust coefficient (non-dimensional normal force, Equation 2.16) be found in Figures 4.13 and 4.14:
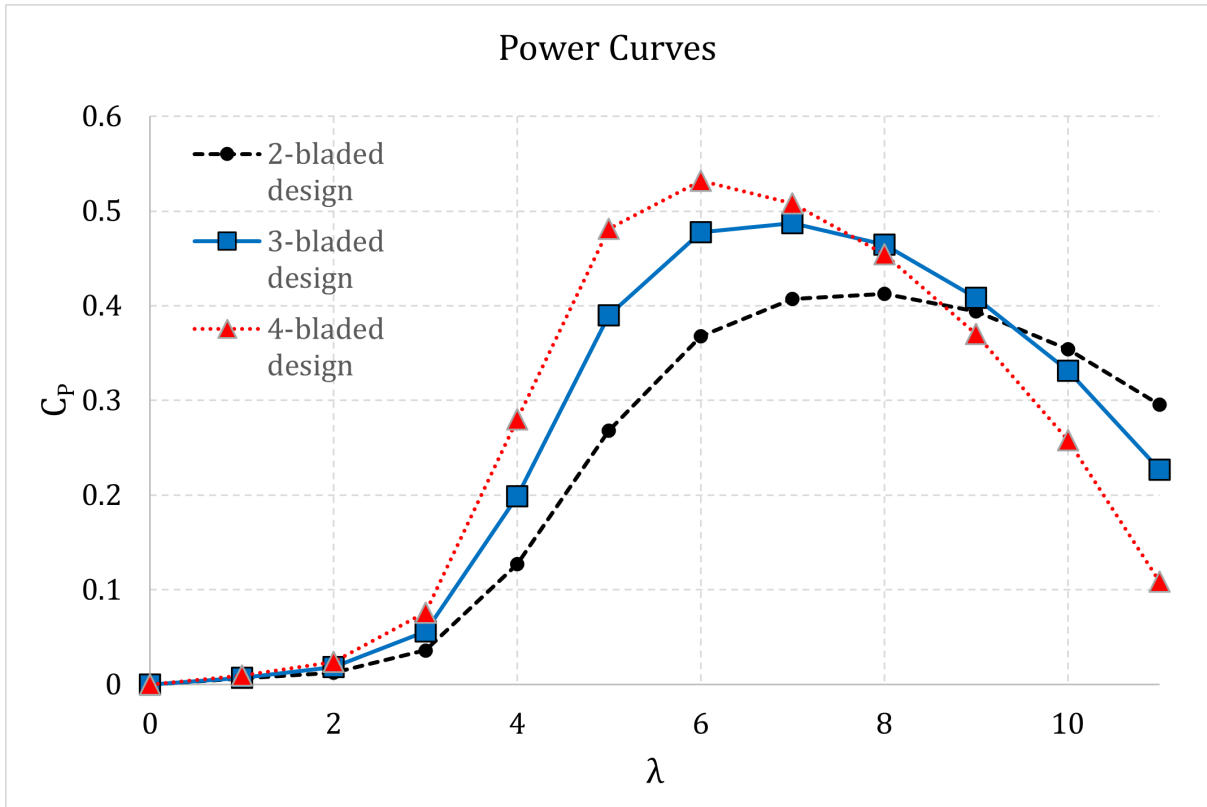
Figure 4.13: Power curves calculated for NREL Phase VI with a boundary layer thickness of 0.32 cm
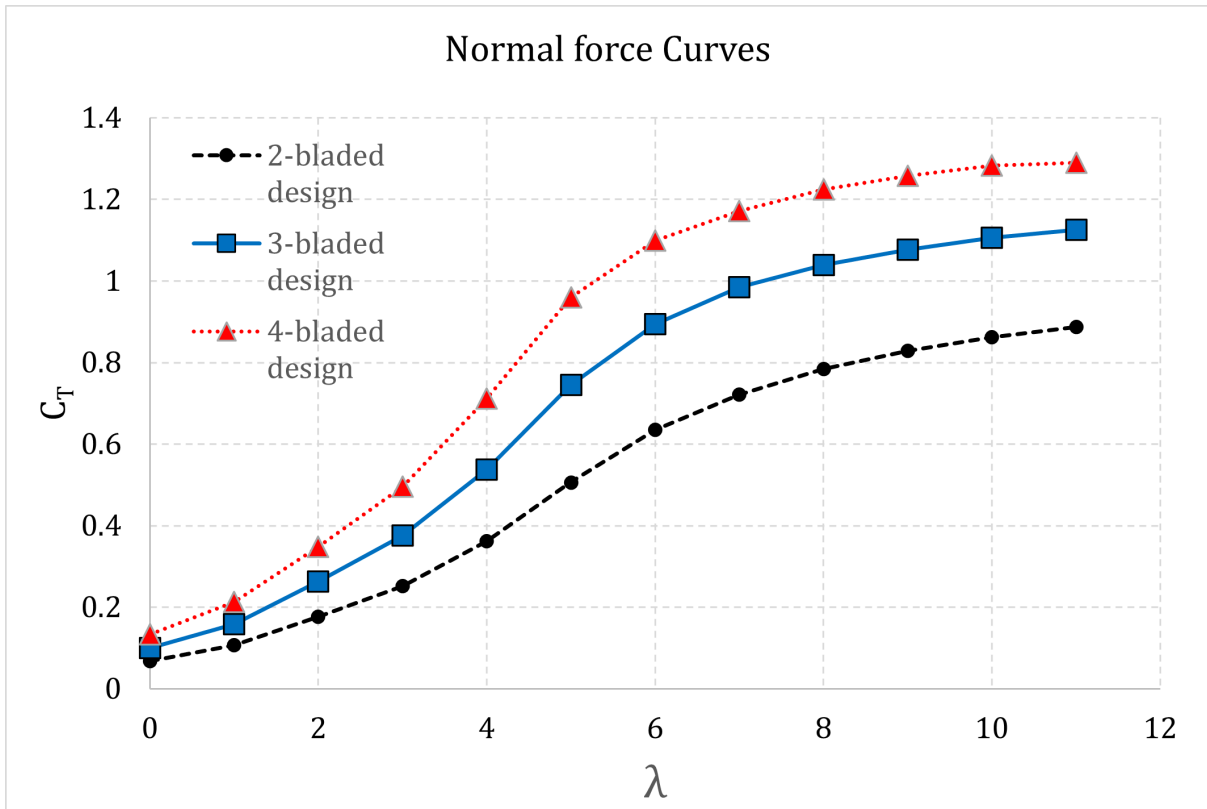

Figure 4.14: Normal force curves calculated for NREL Phase VI with a boundary layer thickness of 0.32 cm

Comparing the different designs, one can see that there is a remarkable increase in power generation between the two-bladed and the three and four-bladed designs ($\sim$ 15%), while there is a small difference between the three and four-bladed ones ($\sim$ 6%), which might give a first idea of the return of investment one may get, being the three bladed, apparently, the best choice regarding manufacturing, maintenance and transportation costs while obtaining an average efficiency of $\sim$ 45% in a wide range of operation, which is a fair high one compared to the Betz limit.

Moreover the optimum points of operation are clear for each model, obtaining greater values for lower λ as the blade number increase, and improving the slope of the C_p graph, which has an important role regarding controllability (Section 3.e).

4.c.i   Model validation

In order to carry out a proper validation study for the rigid body motion simulation, a CAD model that already has been tested experimentally or by other researchers should be used. This would be beneficial because, although similar size turbines should be generating similar magnitudes of power, there can still be vast differences in the exact value due to the design of the blades. It is plausible that one turbine could generate 100 W, while a different turbine with the same radius might generate only 20 W. Therefore, in order to determine the accuracy of a model, a turbine with known or estimated power generation values should be modeled. Thankfully there is a large amount of published research regarding the power generation of the NREL Phase VI turbine in various conditions, so it would be easy to compare the results.

Comparing the two-bladed rotor of Figures 4.13 and 4.14 to the reference ones (Figures 4.15 and 4.16[6]), it can be seen that the values are above the ones referenced from $\lambda = 3$ (for Figure 4.15), however, the force curve (Figure 4.16) is almost the same. Regarding differences, one must take into account the fact that in this study, the hub of the blade started a bit above the plane of symmetry, about 0.2 meters above (Figure 4.17), yielding higher torque results than expected and therefore higher power coefficient calculation. Moreover, the mesh from Togregrosa et al. was of 8M cell, which is expected to yield more accurate results. All in all, the curves are pretty similar in shape, with a maximum power generation at around $\lambda = 8$, the same as the one found in literature.
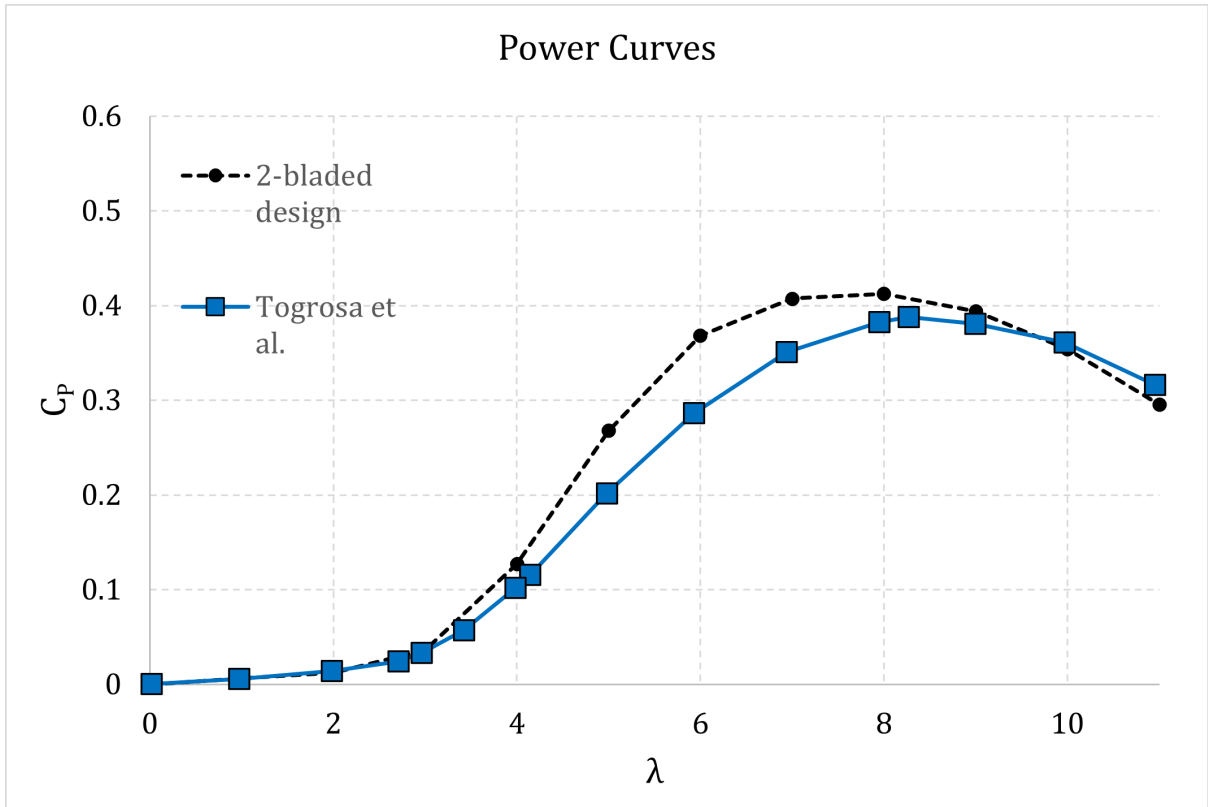
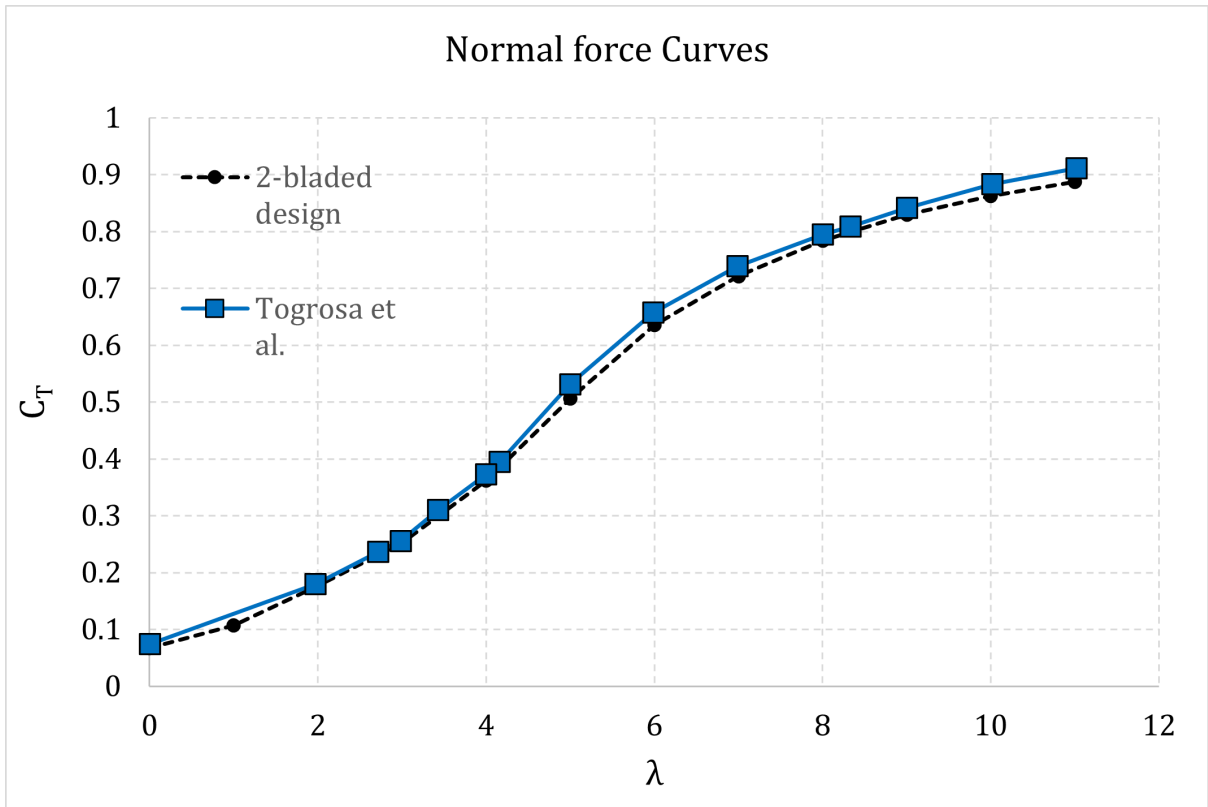**Figure 4.15:** Power curve for the blade NREL Phase VI [6]

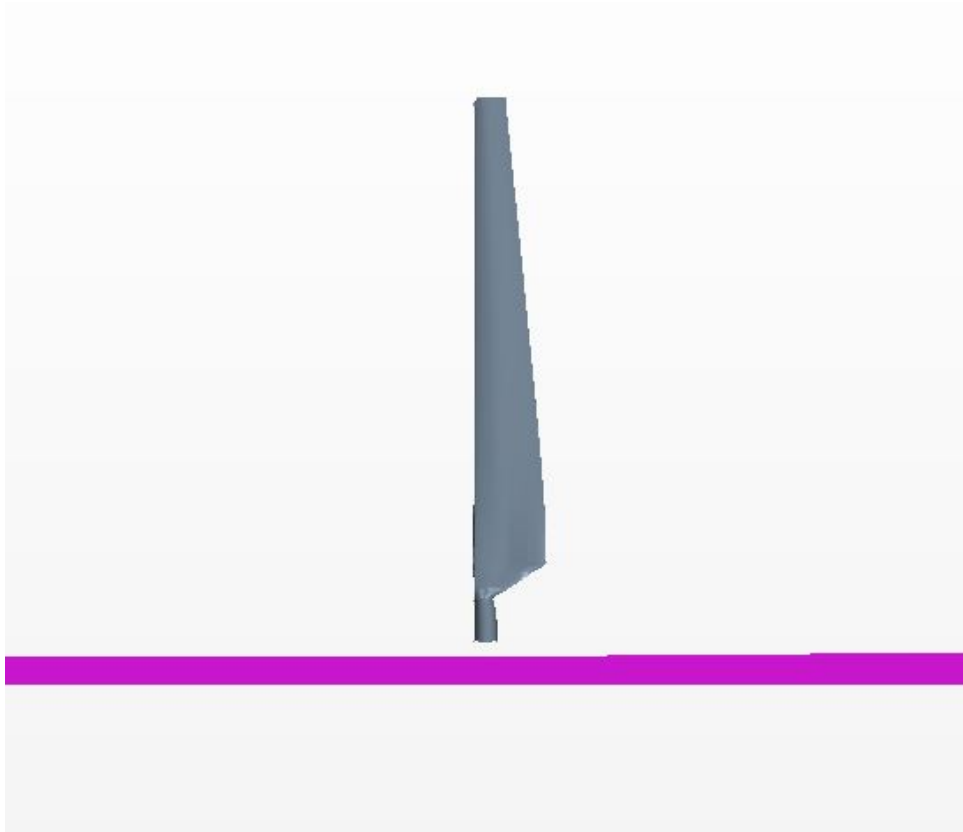**Figure 4.16:** Force curve for the blade NREL Phase VI [6]

Figure 4.17: Gap between hub and symmetry plane (origin)

Moreover, according to Mukesh M. Yelmule et al.[19], the pressure coefficient distribution for a two-bladed wind turbine with the NREL blade at a rotation rate of $\lambda = 4$ has the following solutions (red dots of Figures 4.18 and 4.19), which are plotted with the results of the blade calculated for $\lambda = 4$ (blue dots):
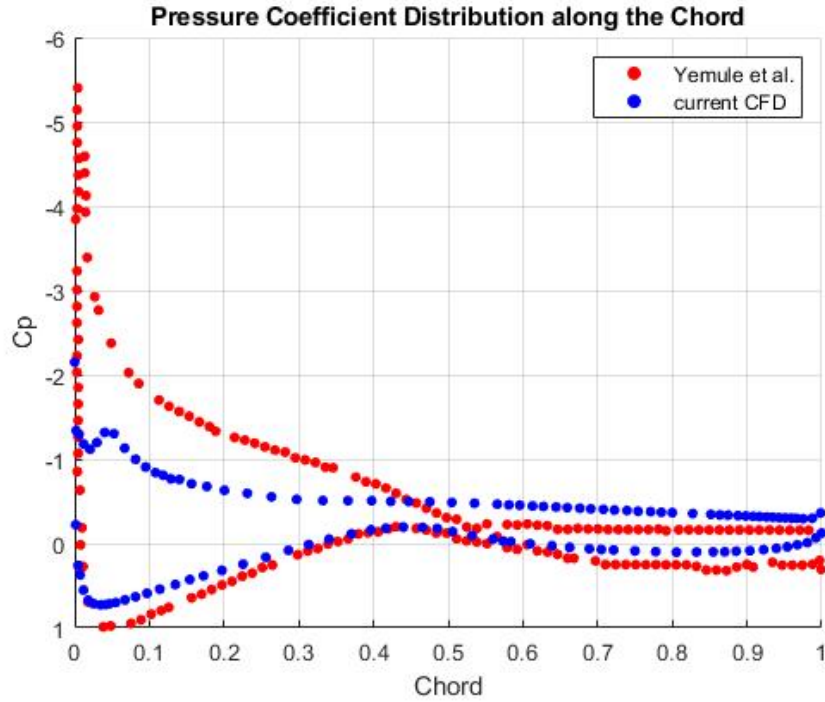
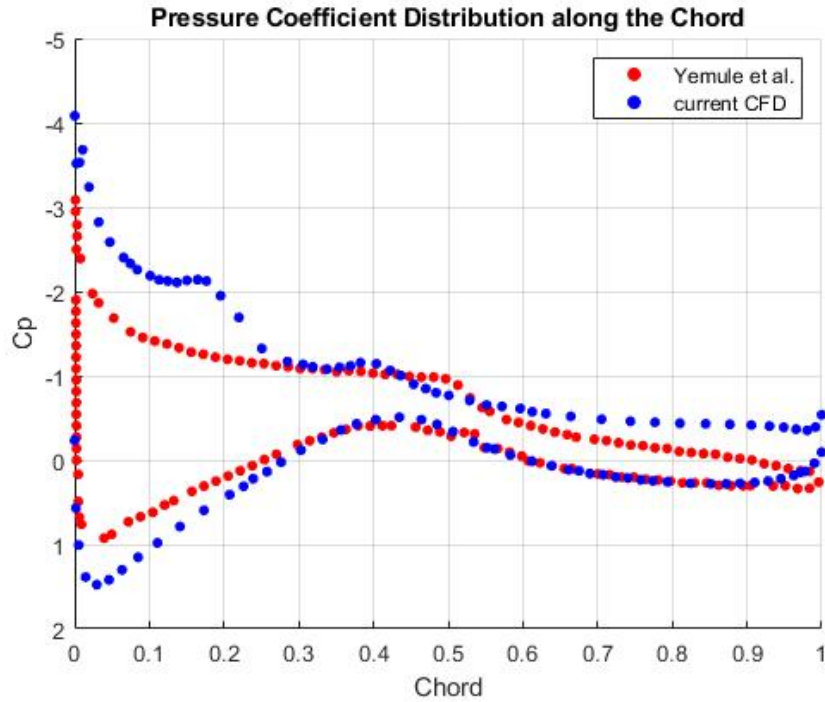**Figure 4.18:** Pressure coefficient distribution at r/R=0.633

Figure 4.19: Pressure coefficient distribution at r/R=0.95

As can be seen in the images, the tip solution is pretty similar, while the 63% is not as similar on the suction side, but might be due to the differences in the atmosphere conditions (in [19] they make use of a density of 1.246 kg/m^3), mesh size (for the 2-bladed model a mesh of $\sim$ 3.6M cell was used), the software (in the Yemule study ANSYS CFX 12.1 was used) or due

63

to the hub gap (Figure 4.17). In addition, the transition from laminar to turbulent flow used by Yemule et al.[19] is modeled using Langtry and Menter correlation based Gamma-Theta transition model, which is property of ANSYS, and therefore a different solver from the one used in Star-CCM+.

Once mesh independence was achieved for the current CFD model and the best mesh was chosen (the one with a boundary layer thickness of 0.32 cm) and a number of 3.6M cells for the two-bladed case, more studies were carried out. In this section three main studies will be presented: a pressure distribution along the blade, a shear stress distribution along the blade and finally a velocity representation along the blade.

4.c.ii   Pressure distributions

For this study, two additional derived planes were created in Star-CCM: one at the 3 m section, and another one at 4.5 m, closer to the tip. All results were studied in these two sections, to analyse the pressure evolution not only along the non-dimensional chord, but along the blade radius.

In addition, two types of graphs were collected for this section in order to better represent the phenomena. The first one is a plot of the pressure coefficient along the chord (for instance Figure 4.20), while the second one is a scene of the same scalar function represented for the whole blade section (for example Figure 4.21).

For the dotted-plots, the 3 m section is the red-dotted one, while the 4.5 m section is blue-dotted, and the upper part of each representation is the suction side of the blade (upper side as well), whereas the lower dots show the pressure side of the blades.
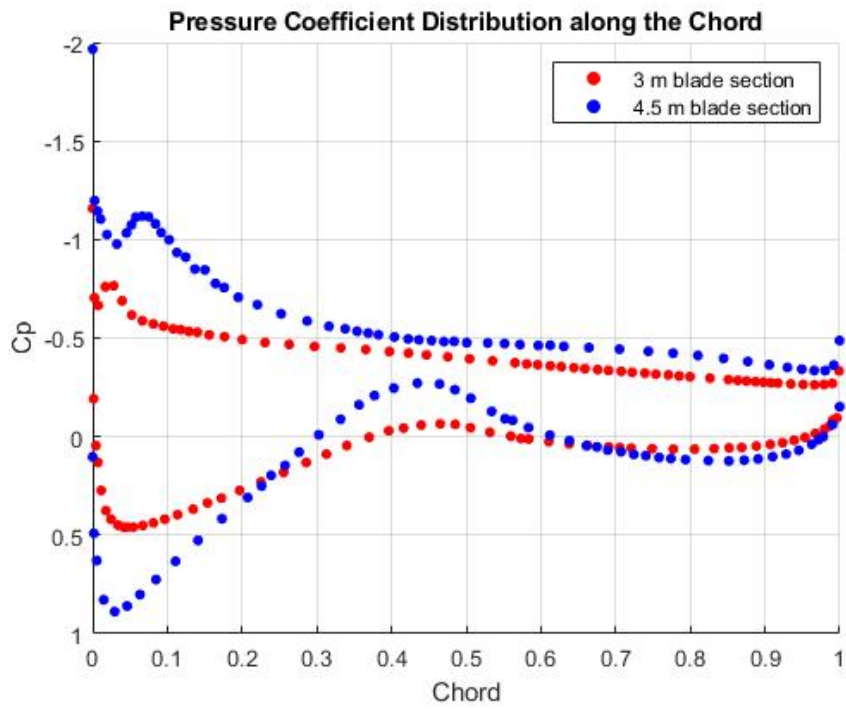
- $\lambda = 3$

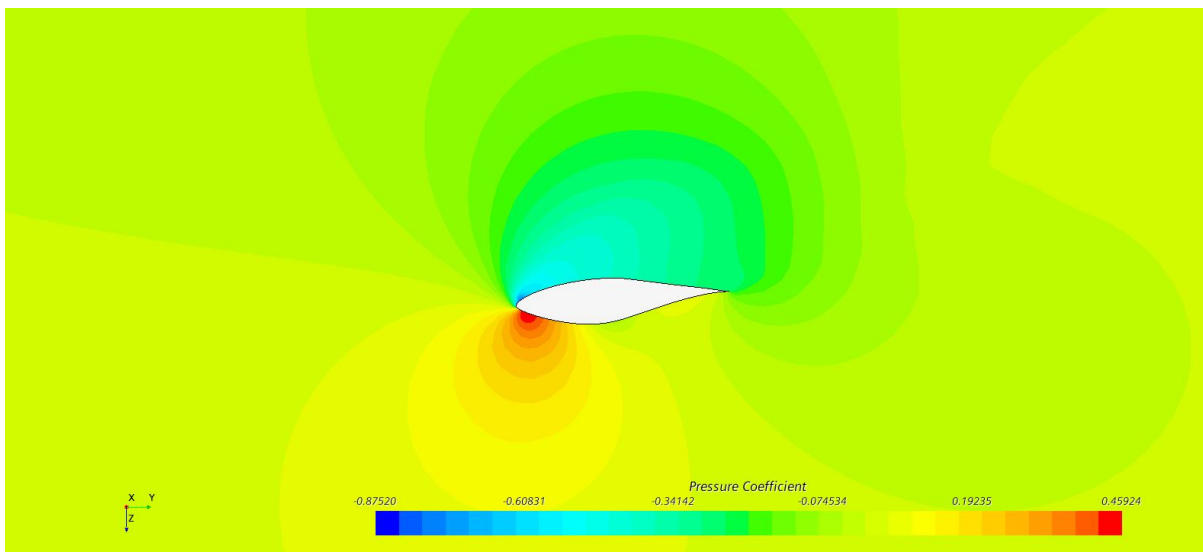**Figure 4.20:** Pressure coefficient for the 3-bladed turbine

Figure 4.21: Pressure coefficient distribution along the 3 m section for the 3-bladed case

Figure 4.22: Pressure coefficient distribution along the 4.5 m section for the 3-bladed case

- $\lambda = 6$

Figure 4.23: Pressure coefficient for the 3-bladed turbine

Figure 4.24: Pressure coefficient distribution along the 3 m section for the 3-bladed case

Figure 4.25: Pressure coefficient distribution along the 4.5 m section for the 3-bladed case

- $\lambda = 9$

Figure 4.26: Pressure coefficient for the 3-bladed turbine

Figure 4.27: Pressure coefficient distribution along the 3 m section for the 3-bladed case
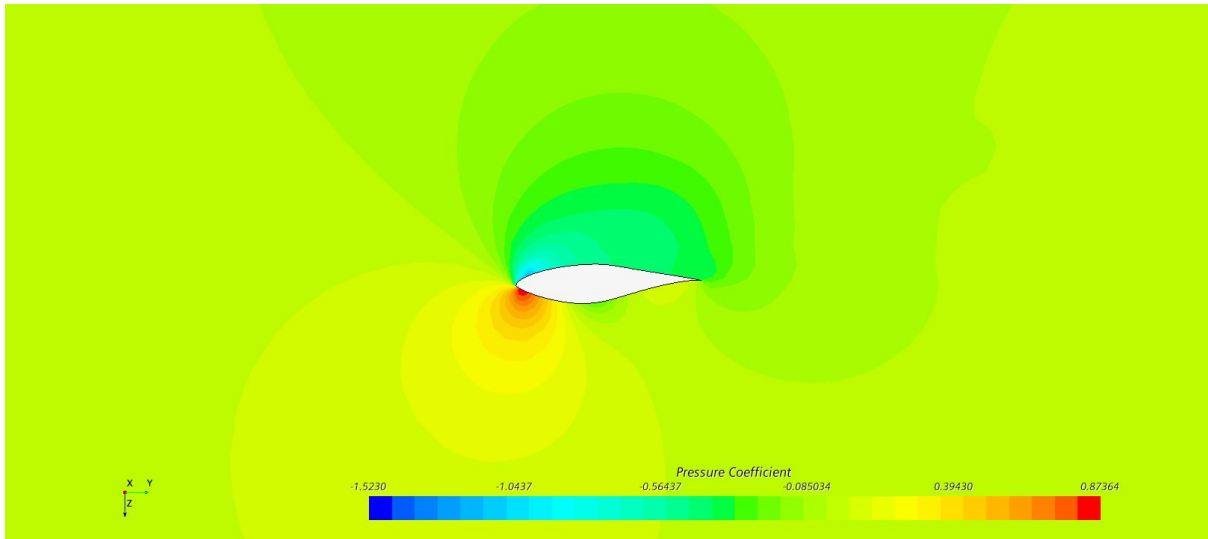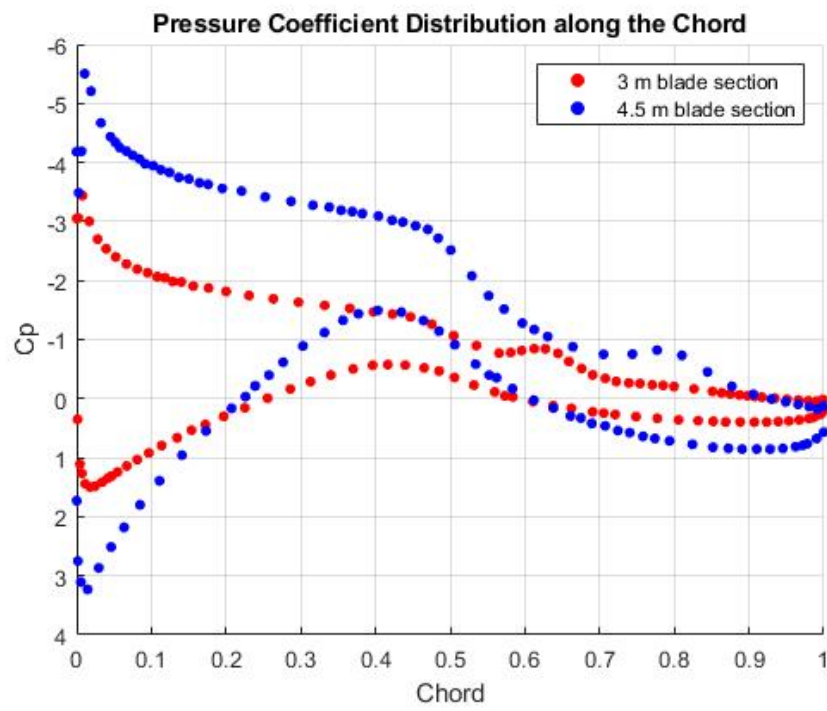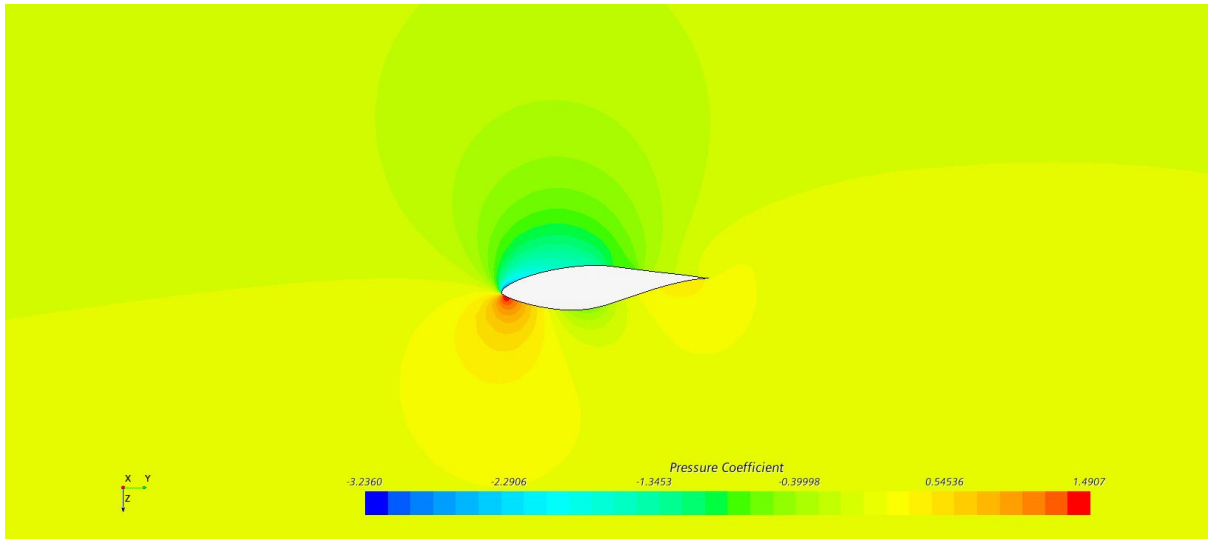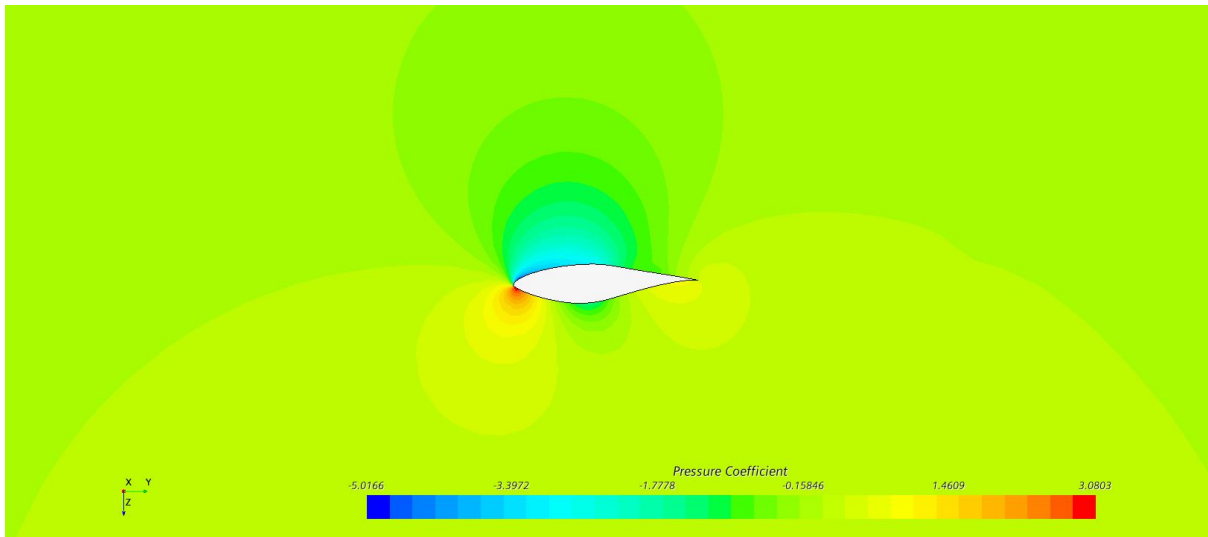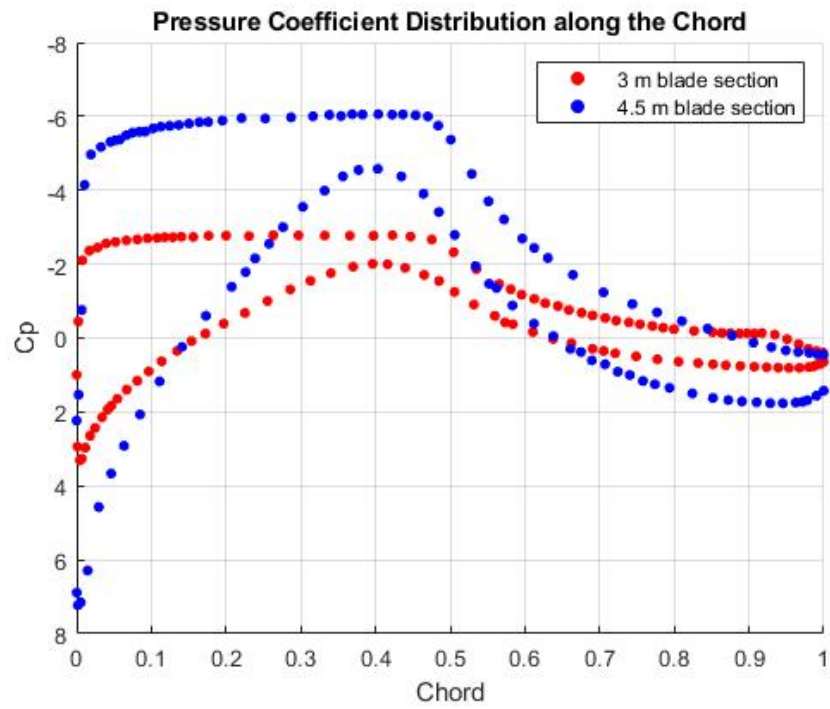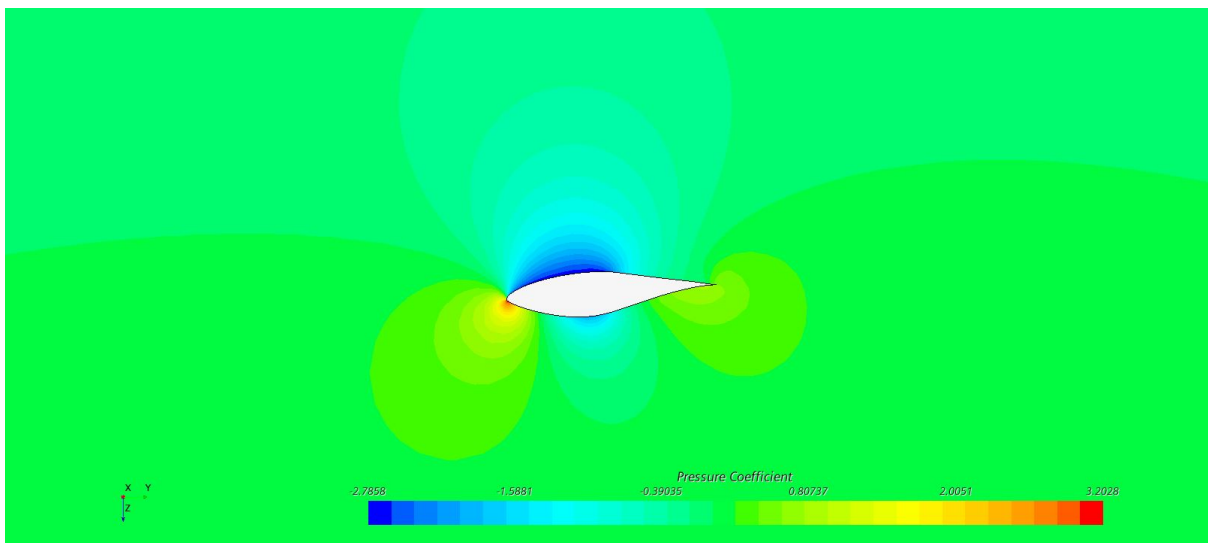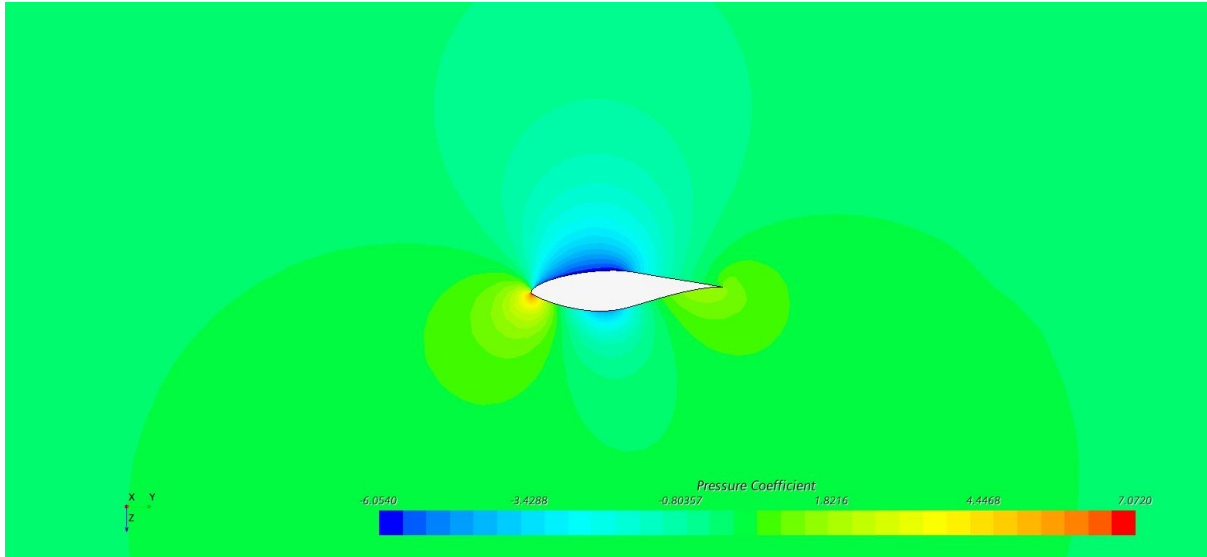
Figure 4.28: Pressure coefficient distribution along the 4.5 m section for the 3-bladed case

For all the cases, it can be seen as the stagnation point advances towards the leading edge for the 4.5 m section (Figures 4.21, 4.22, 4.24, 4.25, 4.27 and 4.28), since it has a lower angle of attack with respect to the hub. The evolution of the suction zone (upper part) becomes larger as the boundary layer is more adhered, up to a certain point, in the onset of stall ($\sim \lambda = 8$), where the efficiency of the airfoil is not the expected one, even though the suction zone remains growing. Entering the stall conditions means that the blade is no longer working efficiently, the increase in the drag is clearly noticeable and thus the energy transformation is poorly done.

Observing the peak in the pressure near the leading edge of the suction surface in Figure 4.23, the peak might be due to flow separation and resulting localized transient stall effects. These graphs are not as precise as the other due to difficulty of RANS models when solving separated and transient flows, however, this does not cause major differences with this flow behaviour, which is a characteristic specific to the S809 airfoil at higher angle of attack, and is in the range of the results of [19]. Figure 4.26 shows a pressure distribution in a regime which is categorized as stall region, where the inertial forces have gained more weight with respect to the viscous ones and the air is in turbulent regime.

Having a look back to the power curves and matching them to the pressure distribution graphs, one can locate the optimum points of operation for the values $\lambda \in [5, 6, 7]$. From $\lambda = 8$, in the 4.5 m section (closer to the tip), the power coefficient value starts to drop, and from that point a different behavior can be seen in the pressure distribution compared with $\lambda = 6$ (Figure 4.26).

4.c.iii Shear stress distribution along blades

For this section, the shear stress has been adimensionalized with the dynamic pressure, yielding better result and therefore being able to clearly observe where the flow is applying greater forces and stresses, and which parts are more exposed to cracking or even breaking (black lines). Moreover, the pressure coefficient has been represented on the extrados of the blades to better observe the flow detachment and evolution. All figures are represented at the section located at 3 m from the hub.

- $\lambda = 3$

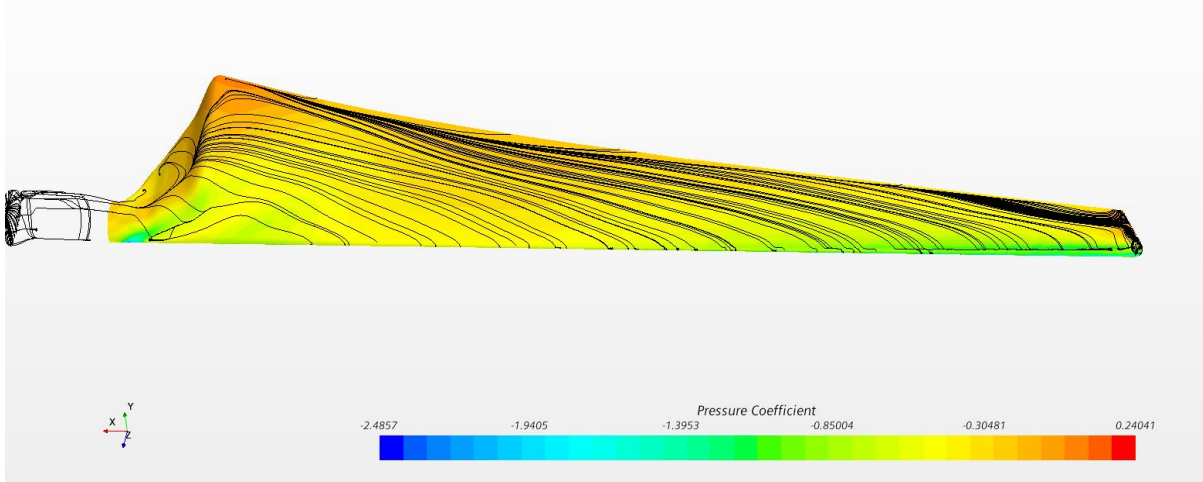**Figure 4.29:** Non-dimensional shear stress and pressure coefficient of a blade in the 3-bladed case
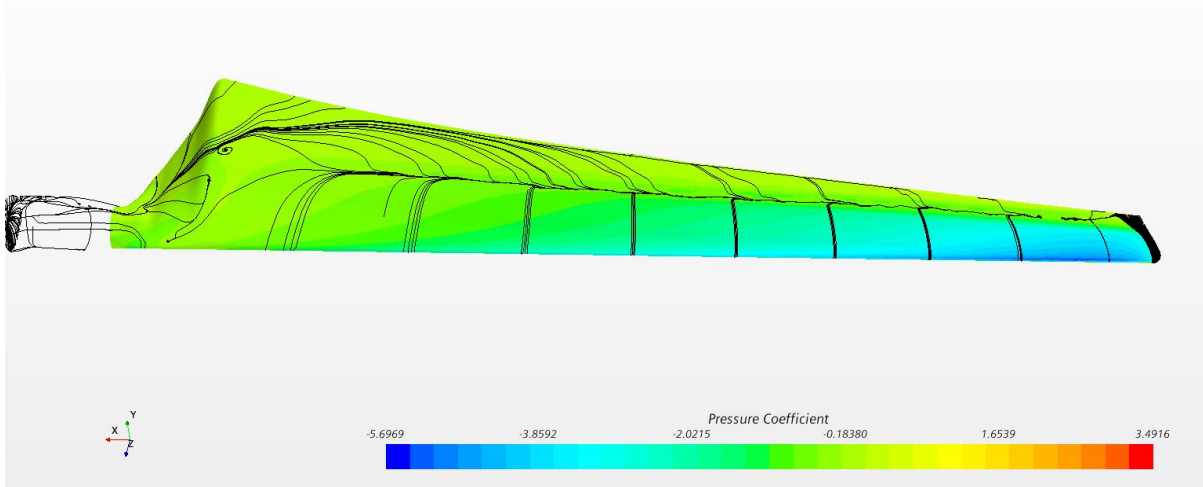
- $\lambda = 6$

Figure 4.30: Non-dimensional shear stress and pressure coefficient of a blade in the 3-bladed case
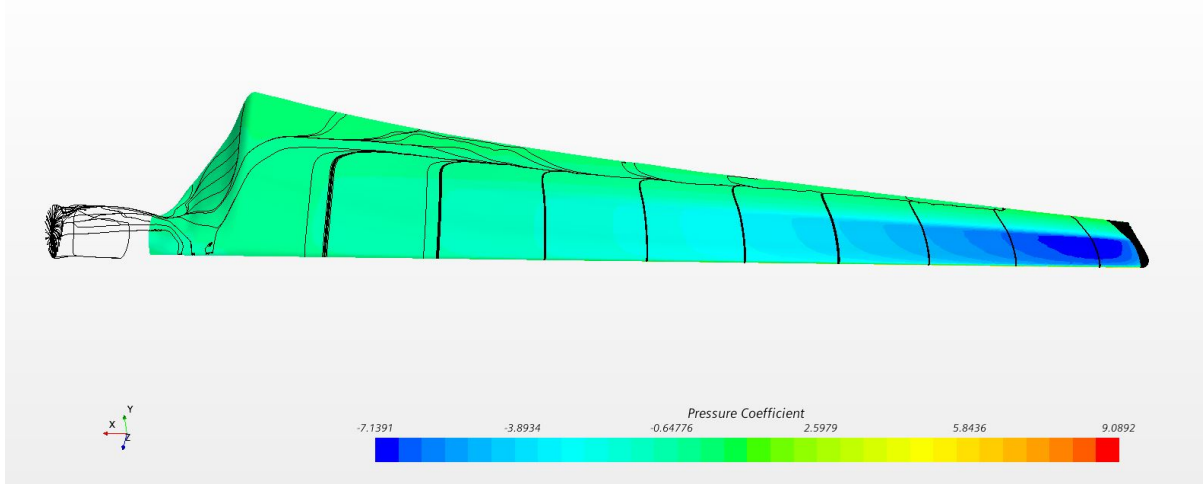
- $\lambda = 9$

Figure 4.31: Non-dimensional shear stress and pressure coefficient of a blade in the 3-bladed case

In these figures, the horizontal black lines like the ones in Figure 4.31 delimit the detachment zone, meaning the flow is not attached to the blade, and therefore exerts null force over it. On the other hand the vertical ones represent the shear stresses that the blade withstands.

At low wind speed the flow is attached, and the transition from laminar to turbulent occurs close to the mid-chord. At the onset of stall separation occurs close to mid chord. In stall, the separation that initiated at mid-chord (at the onset of stall) moves over up to 75% of the chord.

However, following with the pressure distribution ideas, observing the results, one can see how from $\lambda = 7$ the shear stress value starts to increase too much in the tip zone, which is clear in Figure 4.31 (dark blue zones), which could mean that it is not safe for the blade to operate from that point ($\lambda = 7$), since it could increase the maintenance costs if blades had to be replaced regularly due to cracks or other imperfections along the surface.

4.c.iv   Velocity field around sections

Line integral convolution representation was used for this Section, as it provided a nicer and clearer scene of the flow evolution. All scenes are represented at the section located at 3 m from the hub in the rotating reference frame.
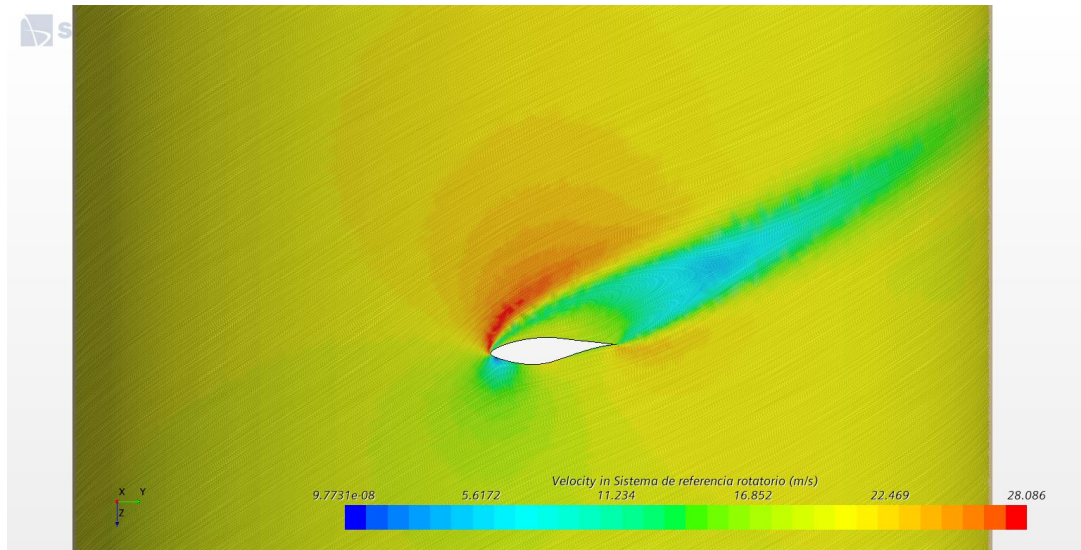
• $\lambda = 3$

Figure 4.32: Velocity field in the 2-bladed case
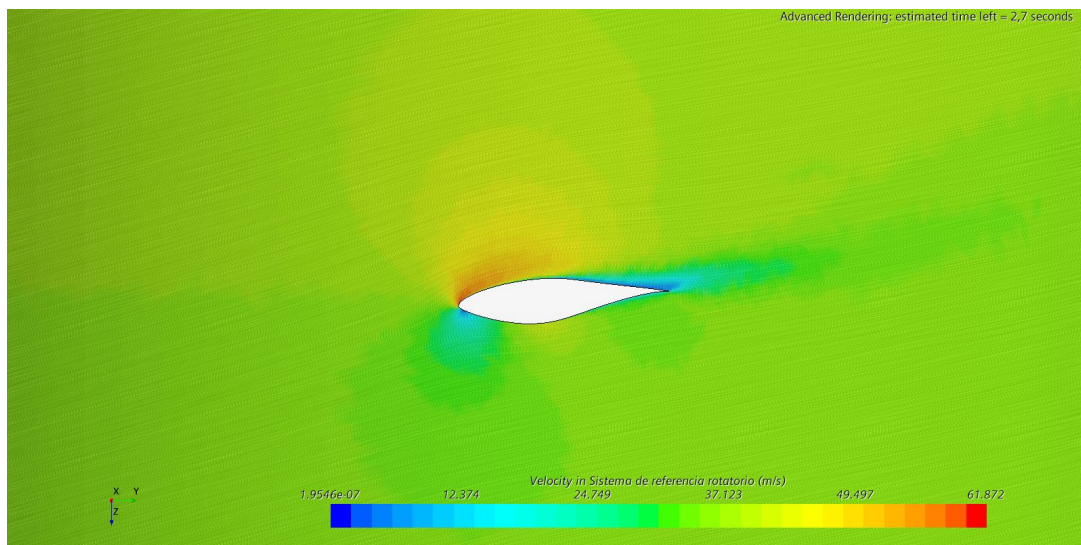
• $\lambda = 6$

Figure 4.33: Velocity field in the 2-bladed case
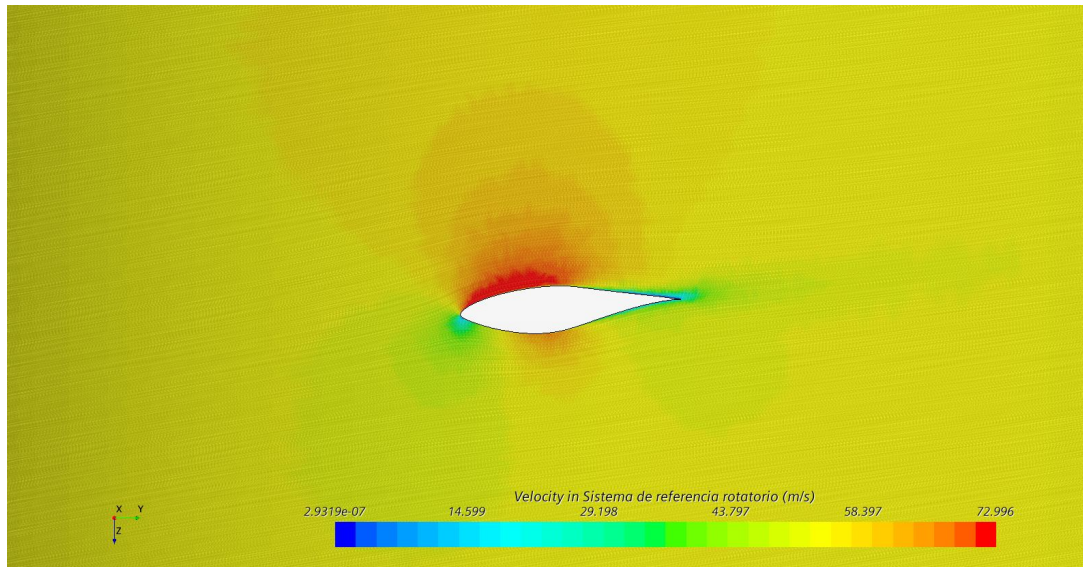
- $\lambda = 9$

Figure 4.34: Velocity field in the 2-bladed case

With pressure and velocity increase there is an increase in the Reynolds number and therefore an increase in the predominant inertial effects over the viscosity ones, which is associated to a small boundary layer near the wall. This is more notable as we increase the λ parameter, since having a look at Figures 4.32, 4.33 and 4.34 one can see how the angle of attack reduces, due to the angular velocity increase (the perceived angle of the blade with respect to the rotational frame gets smaller), and the flow stays attached to the upper part, while for low velocities the angle of attack is increased and the stall conditions can be more easily met at sections closer to the hub, where the twist of the blade induces higher angles of attack. Moreover, observing Figure 4.32, when the flow is laminar, it quickly separates upon reaching the blade, creating a low-pressure wake in the upper part and increasing resistance.

In the CFD analysis, the adhesion of the boundary layer evolution was studied, not being able to distinguish it and observing large eddies at low speeds (up to $\lambda = 5$). In addition, the boundary layer had a behaviour of detaching once the optimum performance point was reached, which varied depending on the speeds. When the flow reaches the end of the blade, a wake is generated where the velocity decreases greatly due to the pressure gradient caused by the sudden change in geometry, increasing resistance as well.

Regarding the optimum operation point, in this section one can see, as previously said, that regarding flow behaviour around the section, the fluid optimum conditions began at $\lambda = 5$, so using this and the previous sections' information, one can estimate that the maximum efficiency and best operation point of the wind turbine would be $\lambda \in [5 - 7]$, being the best one, bearing all the conclusion and conditions in mind, around $\lambda = 6$, or just a bit above that value.

5 Conclusions and future work

Throughout the project, while writing each section, one realizes the real complexity of the problem, which at the beginning might seem simpler, although it has been proved, that even making loads of assumptions, the optimization of modern wind turbines gets way further than a few set of equations. For this study, only the general mechanics and fluid equations were used, without bearing in mind the material resistance nor fatigue conditions (only in the CFD shear stress part), which would increase the difficulty enormously.

However, a wide variety of resources were used to carry out the study, yielding some pretty useful conclusions that may help in the future or even in other different future projects.

First of all, it should be stated that when facing a new wind turbine design, there are several approaches to get a first idea, but the most important thing to care about is power generation. Once the target power has been set, one can get the idea of the size of the blades. Then by making some iterations and using some of the methods presented in this project one can get a pretty advanced design and be able to continue studying the options by more advanced methods like CFD.

Regarding CFD, the first steps when preparing the simulation are essential. Choosing between one or another arrangement of the regions can be very important in terms of not only obtaining good results, but of doing it efficiently, since CFD resources could be extremely expensive (companies often pay millions of Euros for their CFD program licenses), so one must be careful and wise when using them in terms of efficiencies and times. It is very important to define a suitable mesh and be able to refine it in the most optimal way. For instance, the periodicity conditions established saved a lot of CPU resources and time, which for this project might not seem important, but it makes a huge difference in large projects (like in the aeronautical industry).

The mesh, as it has been seen, is vital, since it will be the main obstacle to reaching a solution that is close to reality. It seems obvious that it is easy to choose a mesh to ensure convergence if the geometry is well modeled, however, achieving that using limited computational resources can be much more complicated. One of the major drawbacks when simulating is the time it can take to carry out the simulation, so it is very important to make sure that the simulation is defined correctly, and that the mesh is reasonable for the available resources.

In addition, it is very likely that during the preparation of the simulation the original idea will be lost, forgetting the real physics of the problem. This is important to remember since it can help find results that show that the simulation is not doing what is expected. In addition, when configuring this it is essential to do it in an orderly manner.

To sum up the results of the fluid dynamic modelling and calculations, although the calculated values for power generated by the wind turbines did not exactly match published values, they were within the same magnitude. At low wind speed the flow is attached most of the span, transition from laminar to turbulent occurs close to mid-chord and CFD predictions are correct for these conditions. At the onset of stall separation occurs close to mid chord. Steady state CFD fails to predict the power within measurement range (overprediction of up to 20%) and is known for its difficulty in capturing highly transient effects at the onset of stall. In stall, the separation that initiated at mid-chord (at the onset of stall) moves over up to 75% of the chord. Steady state CFD predicts correctly the quantities within measurement range, although some differences are observed in pressure distribution on the suction side (as stated in Section 4.c.ii), due to the specific stall behavior of the S809 airfoil[19].

In order to improve these models, some inputs for the study can be further defined, such as turbulent viscosity ratio and other flow characteristics, not to mention the inclusion of fluid-structure interaction, where vibrations and material fatigue could be studied more in deep too. Defining as many inputs as possible will certainly improve the accuracy of the CFD. Moreover, it could be interesting to study the unsteady case of this project, to see how transient flows may affect and vary the behavior of the turbine, and even study more the controllability of the rotations, although as introduced in the controllability part (Section 3.e), the left slope of the blade non dimensional power curve is found to be a key design parameter, in order to obtain a design able to produce power in a wide range of wind velocities avoiding the risk of uncontrollable conditions.

Finally, looking back at Figures 4.13 and 4.14, one can see how increasing the number of blades makes the optimum point require a lower wind speed, thus bearing less stresses, but increasing the drag and hence slowing the generation of electricity and becoming less efficient than three-bladed rotors. Two-bladed wind turbines are more prone to a phenomenon known as gyroscopic precession, resulting in a wobbling. Naturally, this wobbling would create further stability issues for the turbine as a whole. This would also place stress on the component parts of the turbine, causing it to wear down over time and become steadily less effective. With three blades, the angular momentum stays constant and in that way the turbine can rotate into the wind smoothly.

All in all, after having studied three types of wind turbines, the three-bladed rotor is the preferred solution, both having the lowest rotational speed (benefiting the acoustic noise emission and blade edge erosion) and having a constant rotational inertia about the yaw axis. Also from an aesthetic point of view (not as important offshore) and without any significant increase in rotor weight (compared to the two-bladed rotor), the three bladed rotor is best fit for most situations. But with the three-bladed rotor occupying a larger three dimensional space compared to the two bladed rotor, the latter may be favourable from a transportation, erection

and maintenance point of view, but as stated in the analysis (Section 4.c), three-bladed design produces in the order of 10% more power than the two-bladed one (although the two-bladed has a higher return on investment). Furthermore, the manufacturing costs of the four-bladed design, in addition to the weight, maintenance and transportation issues, has discarded these type of models from the commercial point of view, since the power generation increase has proven to be unworthy.

6 Project Budget

In this section, the cost calculation of the project development is carried out. This includes the phase of the aerodynamic analysis of the blade without the design costs nor the manufacturing ones, which do not belong to this work. It includes the cost of personnel and computer equipment that are necessary to carry out the work.

6.a Labor costs

This part includes labor, that is to say, the workers who have participated in the project: the student and author of the work, considered a graduate in Aerospace Engineering, and the tutor professor, doctor and graduate in Aerospace Engineering. A cost of 15 €/h has been considered for the student (graduate engineer) and 30 €/h for the tutor. The project has been developed from May 2020 to November 2020, breaking down the student's time in:

- Previous formation, information research and preparation: 70 h.

- Computational study for the different cases: 100 h.

- Analysis of results and document writing: 80 h

For the tutor an estimated time of 30 hours of labor is taken, in which tutorship, analysis of the results and document revision is included.

Concept	Units [h]	Unit cost [€/h]	Cost [€]
Graduate engineer	250	15	3750
Tutor	30	30	900
		Total	4650

Table 4: Labor cost

6.b Cost of computer equipment and software licenses

These costs include the cost of the computers used to carry out the project and the licenses of the software used. Some licenses are for students; therefore, they were free. It has been considered that the Star-CCM+ license has been used for the convergence of the simulations without being computed these hours in the hours of the graduate engineer.

Concept	Units [h]	Unit cost [€/h]	Cost [€]
PC HP Omen (16 GB RAM)			1598.65
Microsoft Office	15	-	Academic license
Simcenter STAR-CCM+ 2020.1	350	3	1050
MATLAB R2018b	20	-	Academic license
Overleaf (Latex)	80	-	Free license
		Total	**2648.65**

Table 5: Cost of computer equipment and software licenses

6.c   Total project budget

Finally, the total project budget is calculated from the sum of the previous breakdowns. In this budget is included the Value Added Tax (VAT) of 21%. All this is reflected in Table 6.

Concept	Cost [€]
Labor cost	4650
Cost of computer equipment and software licenses	2648.65
Subtotal	**7298.65**
VAT (21%)	1532.72
Total	**8831.37**

Table 6: Total project budget

The final cost of the entire project amounts to **EIGHT THOUSAND EIGHT HUNDRED THIRTY ONE EUROS AND THIRTY SEVEN CENTS**.

References

[1] **WindEurope Business Intelligence**
"Wind energy in Europe in 2019. Trends and statistics" (2020), `windeurope.org`.

[2] **A. Betz**
"Introduction to the Theory of Flow Machines" (1966), D. G. Randall, Trans., Pergamon Press, Oxford.

[3] **A. Betz**
"Das Maximum der theoretisch möglichen Ausnutzung des Windes durch Windmotoren" (1920), Journal for the whole turbine industry.

[4] **H. Glauert**
"Airplane Propellers" (1935), in Aerodynamic Theory (Ed. W. F. Durand), Div. L. Chapter XI, Springer Verlag, Berlin.

[5] **James F. Manwell, Jon G. McGowan, Anthony L. Rogers**
"Wind Energy Explained: Theory, Design and Application, 2nd Edition" (2009), John Wiley & Sons Ltd, The Atrium, Southern Gate, Chichester, West Sussex.

[6] **A.J. Torregrosa, A. Gil, P. Quintero, A. Tiseira**
"Enhanced design methodology of a low power stall regulated wind turbine. BEMT and MRF-RANS combination and comparison with existing designs"(2019), Journal of Wind Engineering & Industrial Aerodynamics, Elsevier, Amsterdam.

[7] **Abolfazl Pourrajabian, Peyman Amir Nazmi Afshar, Mehdi Ahmadizadeh, David Wood**
"Aero-structural design and optimization of a small wind turbine blade" (2016), Elsevier, Amsterdam.

[8] **John D. Anderson Jr.**
"Fundamentals of Aerodynamics" (2001), in Aeronautical and Aerospace Engineering Series (Ed. McGraw-Hill).

[9] **D.A. Spera**
"Wind Turbine Technology: Fundamental Concepts of Wind Turbine Engineering" (1994), ASME Press, New York.

[10] **Timmer, W. and Rooij, R.P.J.O.M.**
"Summary of the Delft University Wind Turbine Dedicated Airfoils" (2003), Journal of Solar Energy Engineering-transactions of The Asme - J SOL ENERGY ENG.

[11] **R. Malki, A.J. Williams, T.N. Croft, M. Togneri, I. Masters**
"A coupled blade element momentum – Computational fluid dynamics model for evaluating tidal stream turbine performance" (2012), Marine Energy Research Group, College of Engineering, Swansea University.

[12] **Robert E. Wilson, Peter B. S. Lissaman**
"Applied Aerodynamics of Wind Power Machines" (1974), NTIS, Indiana University.

[13] **O. de Vries**
"Fluid Dynamic Aspects of Wind Energy Conversion" (1979), North Atlantic Treaty Organization, Amsterdam.

[14] **Van Grol, H J, Snel, H, and Schepers, J G.**
"Wind turbine benchmark exercise on mechanic loads: A state of the art report. Volume 1 (Part A): Main body of the report." (1991) , Netherlands.

[15] **Voutsinas, S. G., Rados K. G. and Zervos, A.**
"Wake effects in wind parks: a new modelling approach" (1993) , European Community Wind Energy Conference, Thessalonika.

[16] **Ebert, P. R. and Wood, D. H.**
"Three dimensional measurements in the wake of a wind turbine" (1994) , European Community Wind Energy Conference, Lübeck.

[17] **Marit Reiso**
"The Tower Shadow Effect in Downwind Wind Turbines" (2013), Thesis for the degree of Philosophiae Doctor, Norwegian University of Science and Technology.

[18] **David C. Wilcox**
"Turbulence Modeling for CFD" (1998), Second edition. Anaheim: DCW Industries.

[19] **Mukesh M. Yelmule, EswaraRao Anjuri VSJ**
"CFD predictions of NREL Phase VI Rotor Experiments in NASA/AMES Wind tunnel" (2013), International Journal of Renewable Energy Research.

[20] **Madeline Samuell**
"Computational Fluid Dynamic Modeling and Analysis of Small Scale Horizontal Axis Wind Turbines" (2017), Union College, Schenectady, NY.

[21] **Siemens PLM Software**
"STAR-CCM+ Product Overview" (2017), Siemens Product Lifecycle Management Software Inc.

Wind energy in Europe in 2019 windeurope.org Trends and statistics